Identification of the Induction Motor Parameters at Standstill Including the Magnetic Saturation Characteristics

Sina Khamehchi

School of Electrical Engineering

Thesis submitted for examination for the degree of Master of Science in Technology.

Espoo 23.04.2018

Thesis supervisor:

Prof. Marko Hinkkanen

Thesis advisor:

Eemeli Mölsä, M.Sc. (Tech.)

Aalto University
School of Electrical
Engineering

AALTO UNIVERSITY
SCHOOL OF ELECTRICAL ENGINEERING

ABSTRACT OF THE
MASTER'S THESIS

Author: Sina Khamehchi

Title: Identification of the Induction Motor Parameters at Standstill Including the Magnetic Saturation Characteristics

Date: 23.04.2018 Language: English Number of pages: 8+54

Department of Electrical Engineering and Automation

Professorship: Electric Drives

Supervisor: Prof. Marko Hinkkanen

Advisor: Eemeli Mölsä, M.Sc. (Tech.)

Identification of the induction motor parameters at standstill is studied in this thesis. The main goal of this work is to search for the feasible and applicable speed sensorless self-commissioning schemes. The magnetic saturation of the magnetizing inductance is taken into account. The magnetizing inductance is modeled as a function of the stator flux. Two different identification schemes are chosen based on the literature review. First method uses the single-axis sinusoidal excitation as the test signal. Second method uses the DC-decay test for the magnetizing inductance estimation and DC-biased sinusoidal excitation for the leakage inductance and rotor resistance identification. The DC-decay test is found to be a suitable method for identification of the magnetizing inductance. The single-axis sinusoidal excitation is found to be problematic in the saturation region. The source of the inaccuracy in the single-axis sinusoidal excitation is studied and the reasons are explained. The sensitivity of the schemes to the stator resistance and stator voltage errors is evaluated. Both methods show a very high sensitivity to the stator voltage errors in the case of the magnetizing inductance estimation. However, the DC-decay test shows a lower estimation error in the presence of the stator resistance errors. The estimation of the leakage inductance is robust against the stator voltage errors when the method based on the single-axis sinusoidal excitation is used. The estimation of the rotor resistance using the DC-biased excitation depends on the DC offset current in the presence of both the stator resistance and stator voltage errors.

Keywords: Induction motor drives, linear least squares (LLS), parameter identification, saturation characteristics

Preface

This research work has been carried out at Aalto university, School of Electrical Engineering and Automation. This project has been funded by ABB Oy, as a part of a research on electric drives.

I want to thank my supervisor Prof. Marko Hinkkanen for giving helpful guidance on technical aspects of the research as well as providing constructive advice on scientific writing. I would like to thank my instructor Eemeli Mölsä for his kind support and useful orientation. I also would like to thank the electric drive group members for providing a comfortable and friendly working atmosphere.

Espoo, 23.4.2018

Sina Khamehchi

Contents

Symbols and abbreviations

Matrices and complex space vectors are shown in boldface. Reference parameters are shown with subscript ref.

Symbols

I_s	stator sinusoidal-current amplitude
I_s0	stator DC-bias current
i_a	current of the phase a
i_b	current of the phase b
i_c	current of the phase c
$\boldsymbol{i}_\mathrm{M}$	magnetizing current complex space vector in the Γ model
$\boldsymbol{i}_\mathrm{m}$	magnetizing current complex space vector in the T model
$\boldsymbol{i}_\mathrm{R}$	rotor current complex space vector in the Γ model
$\boldsymbol{i}_\mathrm{r}$	rotor current complex space vector in the T model
$\boldsymbol{i}_\mathrm{s}$	stator current complex space vector
i_α	α-axis component of the stator current
i_β	β-axis component of the stator current
$\boldsymbol{i}'_\mathrm{M}$	magnetizing current complex space vector in the inverse-Γ model
$\boldsymbol{i}'_\mathrm{R}$	rotor current complex space vector in the inverse-Γ model
j	imaginary unit
L_M	magnetizing inductance in the Γ model
L_Mi	incremental inductance
L_m	magnetizing inductance in the T model
$L_{\mathrm{r}\sigma}$	rotor leakage inductance
L_s	stator inductance
$L_{\mathrm{s}\sigma}$	stator leakage inductance
L_σ	leakage inductance in the Γ model
L'_M	magnetizing inductance in the inverse-Γ model
L'_σ	leakage inductance in the inverse-Γ model
N	number of samples
R_R	rotor resistance in the Γ model
R_r	rotor resistance in the T model
R_s	stator resistance
R'_R	rotor resistance in the inverse-Γ model
T_s	switching period
t	time variable
U_dc	DC-bus voltage
U_M	magnetizing sinusoidal-voltage amplitude
U_s	stator sinusoidal-voltage amplitude

U_{s0}	DC-bias stator voltage
$\boldsymbol{u}_{\mathrm{M}}$	magnetizing voltage complex space vector in the Γ model
$\boldsymbol{u}_{\mathrm{s}}$	stator voltage complex space vector
$\boldsymbol{u}_{\mathrm{s,ref}}$	stator reference voltage
$\boldsymbol{X}$	regressor matrix
$\boldsymbol{y}$	vector of the inverse of the magnetizing inductance
Z	complex impedance
α	stator coordinate real component
β	stator coordinate imaginary component
δ_{s}	phase angle between the stator current and stator flux
$\boldsymbol{\varepsilon}$	residual vector
τ_{r}	rotor time constant
τ_{s}	stator time constant
ϕ_{s}	phase angle
$\boldsymbol{\psi}_{\mathrm{s}}$	stator flux complex space vector
ψ_{s}	stator flux magnitude
$\boldsymbol{\psi}_{\mathrm{R}}$	rotor flux complex space vector in the Γ model
$\boldsymbol{\psi}_{\mathrm{r}}$	rotor flux complex space vector in the T model
$\boldsymbol{\psi}'_{\mathrm{M}}$	magnetizing flux space vector in the inverse-Γ model
ψ'_{M}	magnetizing flux magnitude in the inverse-Γ model
ω	angular frequency
ω_{m}	electrical angular speed

Superscripts

$\hat{}$	estimated quantity
T	transpose

Operators

$\int_0^t \mathrm{d}t$	integral with respect to variable t
$\dfrac{\mathrm{d}}{\mathrm{d}t}$	derivative with respect to variable t
$\dfrac{\partial}{\partial y}$	partial derivative with respect to variable y
$\sum_i$	sum over index i

Abbreviations

AC	alternating current
DC	direct current
DFT	discrete Fourier transform
IM	induction motor
LLS	linear least squares
PI	proportional integral
PWM	pulse-width modulation
RLS	recursive least squares

1 Introduction

1.1 Background

Electric machines are electromechanical converters which transform the mechanical energy to electrical or vice versa [1]. Amongst various types of electric machines, induction machines (IM) are the most common machines in industrial applications. Although IMs can be used as motors and generators, their performance as motors is preferred [1]. In these motors, AC current is supplied to the stator and induced to the rotor. Thus, these motors are called the induction motors. These motors are inexpensive, robust and durable. They can be started by direct connections to the mains. IMs are not as efficient as synchronous motors. These motors can be connected to the power converters and be used as variable speed drives.

Various control methods are used to drive IMs. The simplest method is called scalar control (V/f control). This strategy is based on keeping the stator flux constant at different operating points and steady-state equations are used. For this purpose, the stator voltage is varied proportional to the frequency [1]. Scalar control is normally used for simple applications. Vector control strategies, e.g., rotor-flux-oriented vector control and direct torque control are used in the high-performance drive systems [2]. The dynamic system response is fast in the vector control methods and torque can be controlled [3]. In addition, speed measurements can be replaced with speed estimations. All motor states and outputs needed for torque, speed and/or position control feedback are obtained from the estimated flux value in the speed or position sensorless drives [4]. Hence, the stability and the performance of the controller depend on the estimated flux.

Speed sensorless control schemes are often used in general-purpose drives. Control schemes require a knowledge of the motor equivalent circuit parameters and the performance of the controller relies on the accuracy of the motor parameters. Difference between the actual parameters and those used in the controller leads to an undesired inaccuracy in the performance of the controller. In some applications, the motor and inverter are not sold as a unit and the parameters of the motor are not known beforehand [5, 6]. In addition, not all the motor parameters are provided

by the manufacturers. These parameters are estimated by means of measurements during the drive initialization. The initialization implemented by the drive is known as the self-commissioning. Self-commissioning is needed as a starting phase for motor control.

A great number of schemes for motor parameter identification are available in literature. Classical identification process is based on DC, no-load and locked-rotor tests. The no-load test (open-circuit test) is utilized with exciting the motor using a three-phase sinusoidal voltage with the rated frequency [1]. For the locked-rotor test, as the name illustrates, the rotor is blocked to avoid any rotation. The three-phase voltage is fed to the motor as in the no-load test. The no-load test cannot be utilized in several applications where the motor is connected to the load, e.g., rolling mill plants and hoist crane systems and disconnecting the motor from the load might be impossible or costly. Locking the rotor can also be difficult and undesirable. Moreover, the classical tests need skilled operators to be utilized [7]. Consequently, a more appropriate method for motor equivalent circuit parameter identification in several applications would be at standstill.

The magnetic saturation of the inductances is important and should be taken into account. In control schemes, the reference flux changes at different motor operating points. Inductance value is not constant in these operating points due to the magnetic saturation. As the reference changes, the parameters should be updated in the controller. Hence, the saturation characteristic is necessary for the control observers. Also, the resistances of the motor depend on the temperature. The effect of the temperature is not considered in this research.

1.2 Objectives of the Thesis

The purpose of this thesis is to search for the feasible speed sensorless parameter identification schemes at standstill including the magnetic saturation effect. First, dynamic T model is discussed and voltage and flux equations are presented. Alternative Γ and inverse-Γ models of the motor are obtained from the T model. For identification of the motor parameters, Γ model is used as reference. The magnetic saturation of the magnetizing inductance is evaluated and some modeling approaches are discussed. Since the identification of the inverter-fed IMs is studied, the inverter non-linearity and voltage errors caused by the inverter are evaluated and discussed.

In order to search for more applicable methods, some of the parameter identification schemes are reviewed briefly with their excitation signals, properties and drawbacks. The literature review covers a range of estimation methods including the classical tests, self-commission and standstill self-commissioning schemes in order to provide a more appropriate perspective. Some of the methods are discussed in details. Two most promising standstill self-commissioning methods are selected for the implementation and detailed comparison. Robustness of the selected methods against the stator resistance errors and voltage errors is evaluated and compared.

2 Induction Motor Models

Depending on the rotor winding type, IMs are categorized into squirrel-cage type and wound-rotor type. As the name represents, squirrel-cage IMs have embedded bars as winding in the slots of the rotor, short circuited at both ends. Wound-rotor IMs contain a three phase winding on the rotor similar to the stator [1]. From the economical perspective, squirrel-cage IMs are more appropriate and in addition, simpler to be manufactured. Wound-rotor IMs on the other hand, produce smoother torque in addition to an improved magnetomotive force waveform due to the distributed winding of the rotor [1]. Figure 2.1 shows the three-phase stator winding of the motor. Generally, in IMs, the stator is magnetized with variable current. Thus, a rotational magnetic field is produced in the air gap between the stator and rotor. The current that is produced by the winding can be expressed in the space vector form.

2.1 Space Vectors

Space vector representation contains two perpendicular axes. The two perpendicular axes, α and β, produce a coordinate system defined as the stator coordinate system.

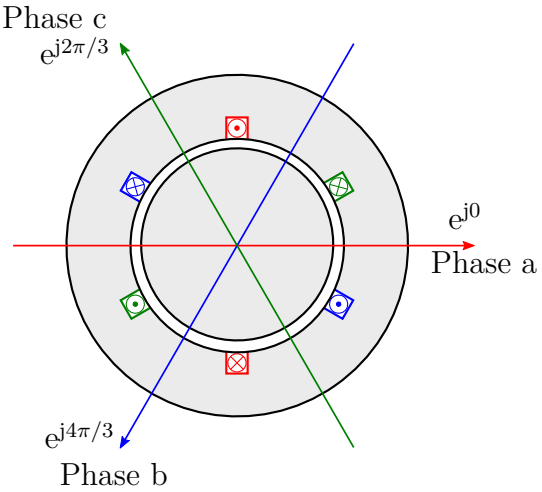

Figure 2.1: Induction motor three-phase winding magnetic axes.

Normally, the zero sequence component is not included since the stator is delta-connected, or the neutral point (star-point) is not connected. Three-phase stator current can be represented in the space vector form as

$$\boldsymbol{i}_\mathrm{s} = \frac{2}{3}\left(i_\mathrm{a} + i_\mathrm{b}\mathrm{e}^{\mathrm{j}2\pi/3} + i_\mathrm{c}\mathrm{e}^{\mathrm{j}4\pi/3}\right) \tag{2.1}$$

where i_a is the current of the phase a, i_b is the current of the phase b, and i_c is the current of the phase c. Voltages and flux linkages can be represented similar to (2.1). Figure 2.2 illustrates the space vector representation of the stator current in the stator coordinates. The stator current complex space vector is

$$\boldsymbol{i}_\mathrm{s} = i_\alpha + \mathrm{j}i_\beta \tag{2.2}$$

where i_α and i_β are the α- and β-axis components of the stator current, respectively.

2.2 Dynamic T Model

The stator voltage space vector in the stator coordinates is

$$\boldsymbol{u}_\mathrm{s} = R_\mathrm{s}\boldsymbol{i}_\mathrm{s} + \frac{\mathrm{d}\boldsymbol{\psi}_\mathrm{s}}{\mathrm{d}t} \tag{2.3}$$

where R_s is the stator resistance and $\boldsymbol{\psi}_\mathrm{s}$ is the space vector of the stator flux linkage. The rotor winding is short circuited at both ends using the end rings [1]. As a result, the rotor voltage equation is given by

$$\boldsymbol{u}_\mathrm{r} = R_\mathrm{r}\boldsymbol{i}_\mathrm{r} + \frac{\mathrm{d}\boldsymbol{\psi}_\mathrm{r}}{\mathrm{d}t} - \mathrm{j}\omega_\mathrm{m}\boldsymbol{\psi}_\mathrm{r} = 0 \tag{2.4}$$

where R_r is the rotor resistance, $\boldsymbol{i}_\mathrm{r}$ is the space vector of the rotor current, ω_m is the rotor electrical angular speed, and $\boldsymbol{\psi}_\mathrm{r}$ is the space vector of the rotor flux linkage.

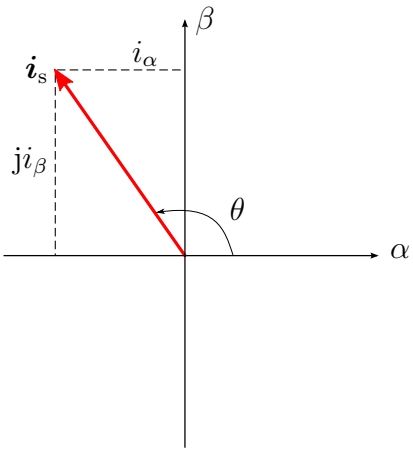

Figure 2.2: Stator current space vector in stator coordinates.

The stator and rotor flux linkages are as follows

$$\boldsymbol{\psi}_\mathrm{s} = L_{\mathrm{s}\sigma}\boldsymbol{i}_\mathrm{s} + L_\mathrm{m}\boldsymbol{i}_\mathrm{m} \tag{2.5a}$$
$$\boldsymbol{\psi}_\mathrm{r} = L_{\mathrm{r}\sigma}\boldsymbol{i}_\mathrm{r} + L_\mathrm{m}\boldsymbol{i}_\mathrm{m} \tag{2.5b}$$

where $L_{\mathrm{s}\sigma}$ is the stator leakage inductance, $L_{\mathrm{r}\sigma}$ is the rotor leakage inductance, and L_m is the magnetizing inductance. The magnetizing current is

$$\boldsymbol{i}_\mathrm{m} = \boldsymbol{i}_\mathrm{s} + \boldsymbol{i}_\mathrm{r}. \tag{2.6}$$

Using (2.3), (2.4) and (2.5) the dynamic T model in Figure 2.3 is obtained. In the T model, the stator inductance is the sum of the magnetizing inductance and stator leakage inductance and defined by

$$L_\mathrm{s} = L_{\mathrm{s}\sigma} + L_\mathrm{m}. \tag{2.7}$$

Similarly, the rotor inductance is the sum of magnetizing inductance and rotor leakage inductance and defined by

$$L_\mathrm{r} = L_{\mathrm{r}\sigma} + L_\mathrm{m}. \tag{2.8}$$

In the T model, the number of parameters is five. This has made the T model an over parameterized model. In addition, in reality, the leakage inductance cannot be divided into two different inductances during the identification [3]. Therefore, other models are obtained from the dynamic T model and used in the control schemes. These models can work as alternatives for the T model since they are mathematically equivalent [8].

2.3 Γ and Inverse-Γ Models

For deriving the Γ model of the motor, a new set of equations is obtained using the scaling factor γ. The rotor current and rotor flux linkage space vectors are

$$\boldsymbol{i}_\mathrm{r} = \gamma\boldsymbol{i}_\mathrm{R} \tag{2.9a}$$
$$\boldsymbol{\psi}_\mathrm{r} = \boldsymbol{\psi}_\mathrm{R}/\gamma \tag{2.9b}$$

where the scaling factor γ can be chosen as

$$\gamma = L_\mathrm{s}/L_\mathrm{m}. \tag{2.10}$$

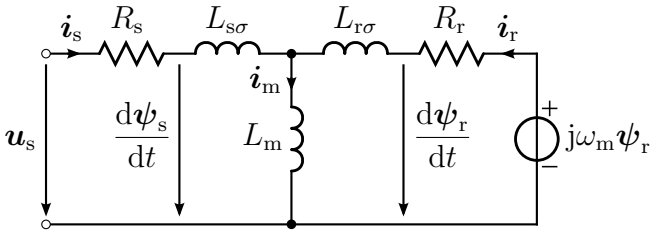

Figure 2.3: Dynamic T model in stator coordinates.

By inserting (2.10) into (2.5), a new set of flux equations is achieved as

$$\boldsymbol{\psi}_\mathrm{s} = (L_{\mathrm{s}\sigma} + L_\mathrm{m})\boldsymbol{i}_\mathrm{s} + \gamma L_\mathrm{m}\boldsymbol{i}_\mathrm{R} \tag{2.11a}$$
$$\boldsymbol{\psi}_\mathrm{R} = \gamma L_\mathrm{m}\boldsymbol{i}_\mathrm{s} + \gamma^2(L_{\mathrm{r}\sigma} + L_\mathrm{m})\boldsymbol{i}_\mathrm{R}. \tag{2.11b}$$

The magnetizing inductance in the Γ model is defined as

$$L_\mathrm{M} = \gamma L_\mathrm{m}, \tag{2.12}$$

the leakage inductance is

$$L_\sigma = \gamma L_{\mathrm{s}\sigma} + \gamma^2 L_{\mathrm{r}\sigma}, \tag{2.13}$$

and the rotor resistance is

$$R_\mathrm{R} = \gamma^2 R_\mathrm{r}. \tag{2.14}$$

The flux linkage equations for the Γ model in stator coordinates are given by

$$\boldsymbol{\psi}_\mathrm{s} = L_\mathrm{M}(\boldsymbol{i}_\mathrm{s} + \boldsymbol{i}_\mathrm{R}) \tag{2.15a}$$
$$\boldsymbol{\psi}_\mathrm{R} = L_\mathrm{M}\boldsymbol{i}_\mathrm{s} + (L_\sigma + L_\mathrm{M})\boldsymbol{i}_\mathrm{R} \tag{2.15b}$$

where $\boldsymbol{\psi}_\mathrm{R}$ and $\boldsymbol{i}_\mathrm{R}$ are the rotor flux and rotor current space vectors, respectively. Figure 2.4 illustrates the dynamic Γ model in stator coordinates.

The dynamic inverse-Γ model can be obtained from the T model as the second alternative equivalent circuit. A new set of rotor equations are obtained as [8]

$$\boldsymbol{i}_\mathrm{r} = \gamma'\boldsymbol{i}'_\mathrm{R} \tag{2.16a}$$
$$\boldsymbol{\psi}_\mathrm{r} = \boldsymbol{\psi}'_\mathrm{R}/\gamma' \tag{2.16b}$$

where the scaling factor γ' is

$$\gamma' = L_\mathrm{m}/L_\mathrm{r}. \tag{2.17}$$

The new flux equations are obtained by inserting (2.17) into the T model flux equations of (2.5) as

$$\boldsymbol{\psi}_\mathrm{s} = (L_{\mathrm{s}\sigma} + L_\mathrm{m})\boldsymbol{i}_\mathrm{s} + \gamma' L_\mathrm{m}\boldsymbol{i}'_\mathrm{R} \tag{2.18a}$$
$$\boldsymbol{\psi}'_\mathrm{R} = \gamma' L_\mathrm{m}\boldsymbol{i}_\mathrm{s} + \gamma'^2(L_{\mathrm{r}\sigma} + L_\mathrm{m})\boldsymbol{i}'_\mathrm{R}. \tag{2.18b}$$

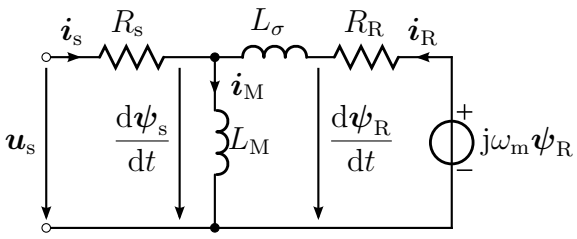

Figure 2.4: Dynamic Γ model in stator coordinates.

Similar to the Γ model, parameters of the inverse-Γ model can be defined. The magnetizing inductance is

$$L'_{\mathrm{M}} = \gamma' L_{\mathrm{m}}, \tag{2.19}$$

the leakage inductance is

$$L'_{\sigma} = L_{\mathrm{s}\sigma} + \gamma' L_{\mathrm{r}\sigma}, \tag{2.20}$$

and the rotor resistance is

$$R'_{\mathrm{R}} = \gamma^2 R_{\mathrm{r}}. \tag{2.21}$$

The inverse-Γ model flux linkage equations in the stator coordinates are given by

$$\boldsymbol{\psi}_{\mathrm{s}} = (L'_{\sigma} + L'_{\mathrm{M}})\boldsymbol{i}_{\mathrm{s}} + L'_{\mathrm{M}}\boldsymbol{i}'_{\mathrm{R}} \tag{2.22a}$$

$$\boldsymbol{\psi}'_{\mathrm{R}} = L'_{\mathrm{M}}\boldsymbol{i}_{\mathrm{s}} + L'_{\mathrm{M}}\boldsymbol{i}'_{\mathrm{R}} \tag{2.22b}$$

where $\boldsymbol{\psi}'_{\mathrm{R}}$ and $\boldsymbol{i}'_{\mathrm{R}}$ are the rotor flux and rotor current space vectors, respectively. Figure 2.5 shows the dynamic inverse-Γ model.

Parameters of the Γ model can be transformed into those of the inverse-Γ model by means of the scaling factor γ_1 as [9]

$$\gamma_1 = \frac{L_{\mathrm{M}}}{L_{\mathrm{M}} + L_{\sigma}} \tag{2.23}$$

where the magnetizing inductance is obtained by

$$L'_{\mathrm{M}} = \gamma_1 L_{\mathrm{M}}, \tag{2.24}$$

the leakage induce is obtained by

$$L'_{\sigma} = \gamma_1 L_{\sigma}, \tag{2.25}$$

and the rotor resistance is obtained by

$$R'_{\mathrm{R}} = \gamma_1^2 R_{\mathrm{R}}. \tag{2.26}$$

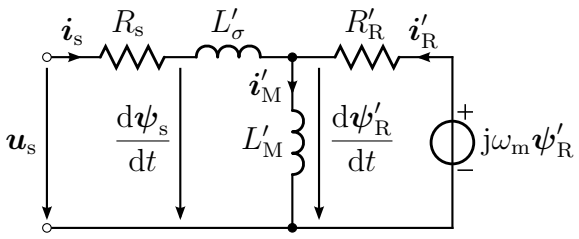

Figure 2.5: Dynamic inverse-Γ model in stator coordinates.

Similarly, the inverse-Γ parameters can be transformed into those of the Γ model using the scaling factor γ_2 as

$$\gamma_2 = \frac{L'_\mathrm{M} + L'_\sigma}{L'_\mathrm{M}} \tag{2.27}$$

where the magnetizing inductance is obtained by

$$L_\mathrm{M} = \gamma_2 L'_\mathrm{M}, \tag{2.28}$$

the leakage inductance is obtained by

$$L_\sigma = \gamma_2 L'_\sigma, \tag{2.29}$$

and the rotor resistance is obtained by

$$R_\mathrm{R} = \gamma_2^2 R'_\mathrm{R}. \tag{2.30}$$

2.4 Motor Model at Standstill

Identification procedure is aimed to be completely utilized at standstill using the Γ model. In addition, excitation is along one axis (e.g., $\boldsymbol{u}_\mathrm{s} = u_\alpha + \mathrm{j}0$). At standstill, ω_m in Figure 2.4 equals to zero. Figure 2.6 shows the dynamic Γ model at standstill. The voltage equations at standstill in stator coordinates are given as

$$\frac{\mathrm{d}\boldsymbol{\psi}_\mathrm{s}}{\mathrm{d}t} = \boldsymbol{u}_\mathrm{s} - R_\mathrm{s}\boldsymbol{i}_\mathrm{s} \tag{2.31a}$$

$$\frac{\mathrm{d}\boldsymbol{\psi}_\mathrm{s}}{\mathrm{d}t} = -R_\mathrm{R}\boldsymbol{i}_\mathrm{R} \tag{2.31b}$$

and based on (2.15) and (2.31), the state-space matrices are obtained as

$$\begin{bmatrix} \frac{\mathrm{d}\boldsymbol{\psi}_\mathrm{s}}{\mathrm{d}t} \\ \frac{\mathrm{d}\boldsymbol{\psi}_\mathrm{R}}{\mathrm{d}t} \end{bmatrix} = \begin{bmatrix} 0 & 0 \\ \frac{R_\mathrm{R}}{L_\sigma} & -\frac{R_\mathrm{R}}{L_\sigma} \end{bmatrix} \begin{bmatrix} \boldsymbol{\psi}_\mathrm{s} \\ \boldsymbol{\psi}_\mathrm{R} \end{bmatrix} + \begin{bmatrix} 1 \\ 0 \end{bmatrix} (\boldsymbol{u}_\mathrm{s} - R_\mathrm{s}\boldsymbol{i}_\mathrm{s}) \tag{2.32a}$$

$$\begin{bmatrix} \boldsymbol{i}_\mathrm{s} \\ \boldsymbol{i}_\mathrm{R} \end{bmatrix} = \begin{bmatrix} \frac{L_\mathrm{M} + L_\sigma}{L_\mathrm{M} L_\sigma} & -\frac{1}{L_\sigma} \\ -\frac{1}{L_\sigma} & \frac{1}{L_\sigma} \end{bmatrix} \begin{bmatrix} \boldsymbol{\psi}_\mathrm{s} \\ \boldsymbol{\psi}_\mathrm{R} \end{bmatrix}. \tag{2.32b}$$

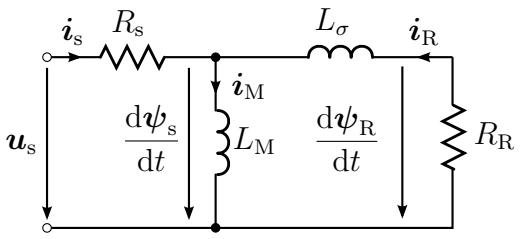

Figure 2.6: Γ equivalent circuit at standstill.

2.5 Magnetic Saturation

The magnetic saturation has a significant effect on the controller performance. The magnetic saturation is essential and should be taken into account when, for instance, the field-weakening or loss-minimizing flux level control is needed [9, 10]. In the rated operating point, IMs are saturated magnetically due to their design for producing maximum torque [11]. In addition, in the field-weakening region where the stator flux decreases, the stator inductance increases. Therefore, inductances of the motor depend on the magnetic state and vary in different operating points.

In the Γ model, the magnetizing inductance L_M can be modeled as a function of the stator flux and the leakage inductance L_σ can be considered constant [9]. Various mathematical models for the saturation characteristics can be found in literature. A polynomial function is used to introduce the saturation curve in [12] and a tangent hyperbolic function is introduced in [13]. A simple rational function is used here as [14, 15]

$$L_\mathrm{M}(\psi_\mathrm{s}) = \frac{L_\mathrm{u}}{1+(\beta\psi_\mathrm{s})^S} = \frac{1}{c_0 + c_s\psi_\mathrm{s}^S} \tag{2.33}$$

where L_u is the unsaturated inductance, β is a non-negative coefficient, S is a positive exponent, and $\psi_\mathrm{s} = |\boldsymbol{\psi}_\mathrm{s}|$ is the stator flux magnitude. Exponent S determines the shape of the saturation characteristic and is normally in the range of $5 \leq S \leq 9$ [16]. When $\psi_s = 1/\beta$, the magnetizing inductance L_M has half of the unsaturated inductance value L_u [17]. Coefficient c_0 is the inverse of the unsaturated inductance and c_s is a positive coefficient. Two inductance forms can be used for defining the relation between the magnetizing current and magnetizing flux assuming that the saturation occurs in the magnetizing branch only. The model in (2.33) stands for the chord-slope inductance. The chord-slope inductance relates the response of the main flux to the variations of the magnetizing current angle [3], i.e.,

$$L_\mathrm{M}(\psi_\mathrm{s}) = \frac{\psi_\mathrm{s}}{i_\mathrm{M}(\psi_\mathrm{s})}. \tag{2.34}$$

Second representation is the incremental or differential inductance. In an operating point (e.g., P), the incremental inductance is defined as the relation between the variations of the flux and magnetizing current, i.e., the tangent of the saturation curve. The incremental inductance is obtained by

$$L_\mathrm{Mi}(\psi_\mathrm{s}) = \frac{\partial\psi_\mathrm{s}}{\partial i_\mathrm{M}(\psi_\mathrm{s})} = \frac{1}{c_0 + (S+1)c_\mathrm{s}\psi_\mathrm{s}^S} \tag{2.35}$$

where c_0, c_s and S are the same coefficients introduced in (2.33) [18]. Figure 2.7 illustrates two representations for the magnetizing inductance. Figure 2.8 shows the chord-slope and incremental inductances as a function of the stator flux for the 2.2-kW motor.

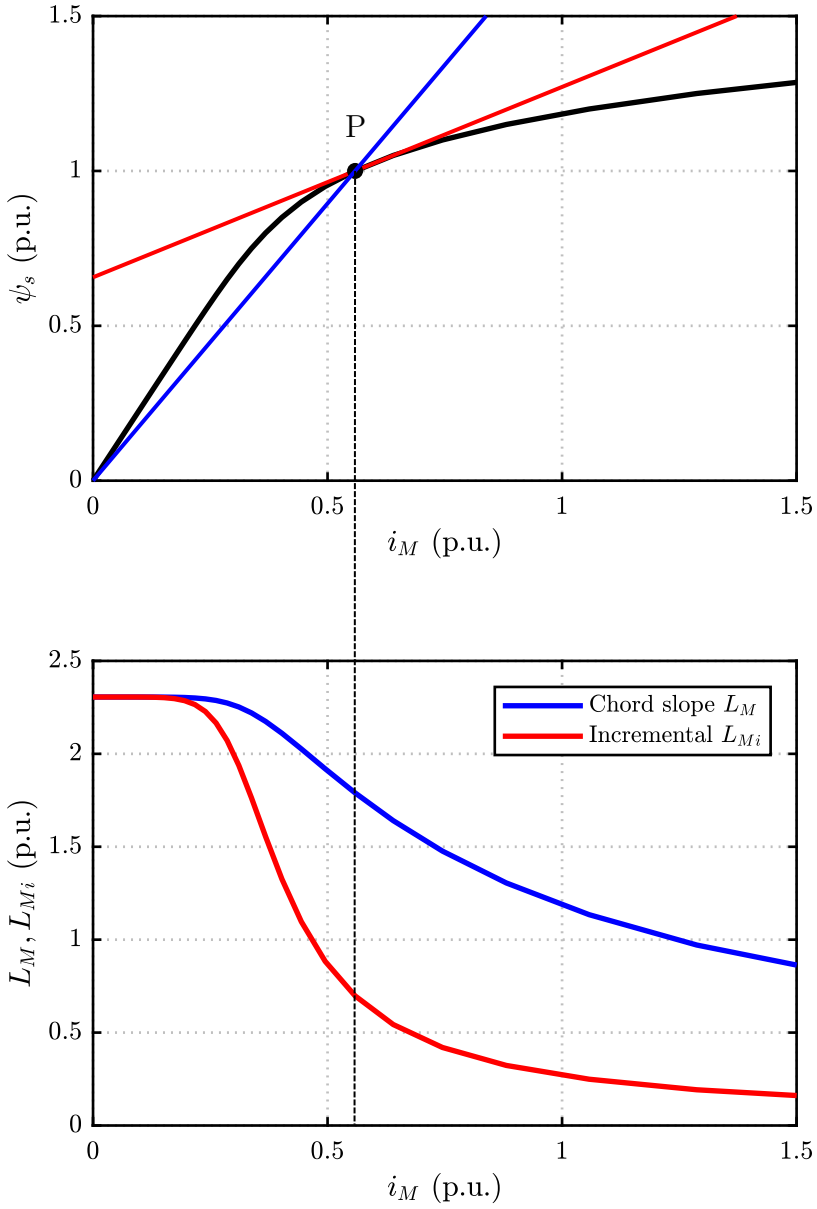

Figure 2.7: The chord-slope and incremental inductances in a certain operating point P.

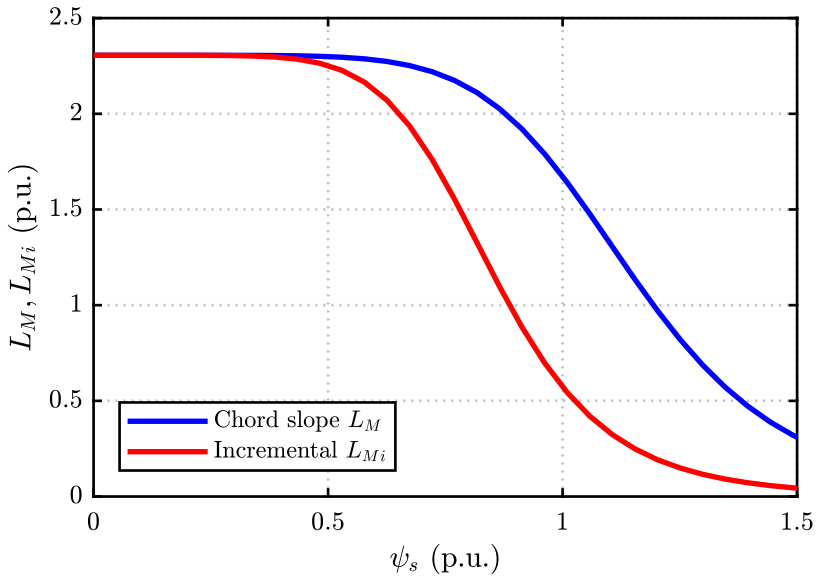

Figure 2.8: The chord-slope and incremental inductances as a function of stator flux for $L_{\mathrm{u}} = 2.31$ p.u., $\beta = 0.87$, and $S = 7$.

2.6 Ratings and Parameters of the Motor

All the simulations are utilized using a 2.2-kW four-pole IM. The motor SI and per-unit ratings and parameters are given in Table 2 based on the data obtained from [9].

2.7 Inverter Non-Linearity

In the identification procedure, IM is fed by a Pulse-width-modulated (PWM) three-phase inverter. In the inverter-fed drives, the voltage gain is nonlinear due to the non ideal characteristics of the inverter [19–21]. Figure 2.9 shows the structure of a three-phase inverter. The DC-link in Figure 2.9 can be short-circuited if both switches in one of the inverter legs conduct at the same time. This phenomenon is referred to as the inverter bridge shoot-through. Therefore, a very short delay is added to the command for the switch that is turning on. This delay is called the dead time or the blanking time. The dead-time produces a phase voltage error from the PWM reference signal. In one of the phases of the inverter e.g., phase a, both switches S_1 and S_2 can be changed from on to off or vice versa simultaneously. This simultaneous switching is considered as the ideal condition. In practice, the dead time t_Δ is added to the on/off procedure of the switches. During the dead time, switches S_1 and S_2 are not conducting. Depending on the direction of the current, either D_1 or D_2 conducts. If the current direction is positive (current flows to the load), D_2 conducts. When the current is negative, D_1 conducts. Figure 2.10 shows one switching period of the inverter where the comparison between a triangular wave (carrier wave) and the duty cycle of the switches d determines the control signal for the switches [22]. The output voltage u_{aN} in Figure 2.10 is changed when the

Table 2: Motor ratings and parameters

Symbol	Parameter	SI Value	p.u. Value
P_N	Power	2.2 kW	1
U_N	Voltage	400 V	1
f_N	Frequency	50 Hz	1
I_N	Current	5 A	1
n	Speed	1436 rpm	-
R_s	Stator resistance	3 Ω	0.065
R_R	Rotor resistance	1.85 Ω	0.040
L_σ	Leakage inductance	25 mH	0.17
L_u	Unsaturated inductance	-	2.31
S	Coefficient	7	7
β	Coefficient	0.84	0.87

blanking time t_Δ is added. This change depends on the direction of the current i_a. It can be seen that the output voltage u_aN is decreased when the current is positive ($i_\mathrm{a} > 0$) and increased when the current is negative ($i_\mathrm{a} < 0$). Taking the dead time into account, the output voltage u_aN can be derived by

$$u_\mathrm{aN} = u_\mathrm{aN,ref} - \mathrm{sign}(i_\mathrm{a})\frac{t_\Delta}{T_\mathrm{s}}U_\mathrm{dc} \tag{2.36}$$

where $u_\mathrm{aN,ref}$ is the reference output voltage, T_s is the switching period, and U_dc the DC-bus voltage [22, 23].

Another source of the inverter non-linearity is the voltage drop caused by the switches and diodes when conducting [23]. This voltage drop can be modeled as a resistive drop by

$$u = R_\mathrm{th} i_\mathrm{a} + u_\mathrm{th} \tag{2.37}$$

where R_th is the dynamic resistances of the switch and diode and u_th is the switch and diode threshold voltage. The dynamic resistances of the switches can be added to the stator resistance in the identification process [24]. Thus, by considering the blanking time in (2.36) and the voltage drop in (2.7) the actual output voltage is obtained by

$$u_\mathrm{aN} = u_\mathrm{aN,ref} - \mathrm{sign}(i_\mathrm{a})\frac{t_\Delta}{T_\mathrm{s}}U_\mathrm{dc} - \mathrm{sign}(i_\mathrm{a})(R_\mathrm{th} i_\mathrm{a} + u_\mathrm{th}). \tag{2.38}$$

To avoid the break points of the signum function in (2.38), it can be replaced by an arctan function as

$$u_\mathrm{aN} = u_\mathrm{aN,ref} - \frac{2t_\delta}{\pi T_\mathrm{s}}U_\mathrm{dc}\arctan\left(\frac{i_\mathrm{a}}{i_\delta}\right) \tag{2.39}$$

where the shape of the arctan function which is determined by i_δ and t_δ takes both the voltage drop and dead time into account. The arctan function multiplied to $2/\pi$ approaches the signum function as i_δ approaches zero [9]. Figure 2.11 represents an example plot of the inverter non-linearity considering the blanking time and voltage drop of the switch using (2.39).

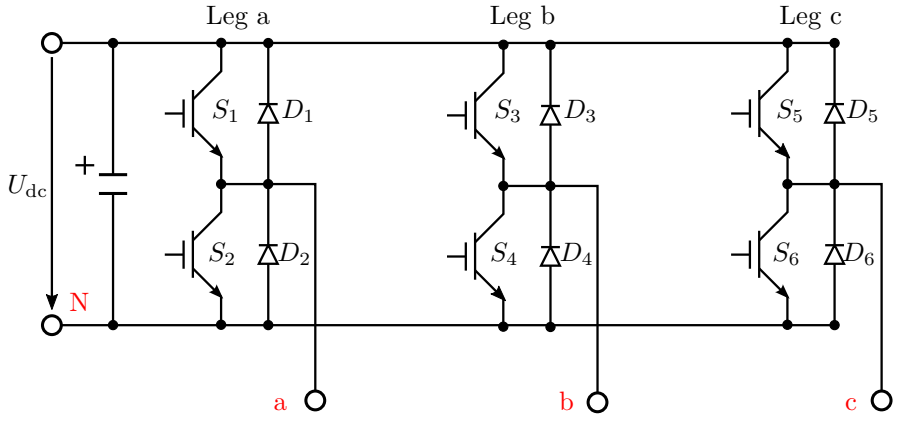

Figure 2.9: Schematic of a three-phase inverter.

In the identification procedure, the stator voltage is reconstructed by means of the DC-link voltage and switching duty cycles since the equipment for measuring the stator voltage terminals is not included in the standard drives. Thus, the voltage distortion caused by the dead-time, and the semiconductor voltage drop produce an error when the actual and reconstructed reference voltage are compared.

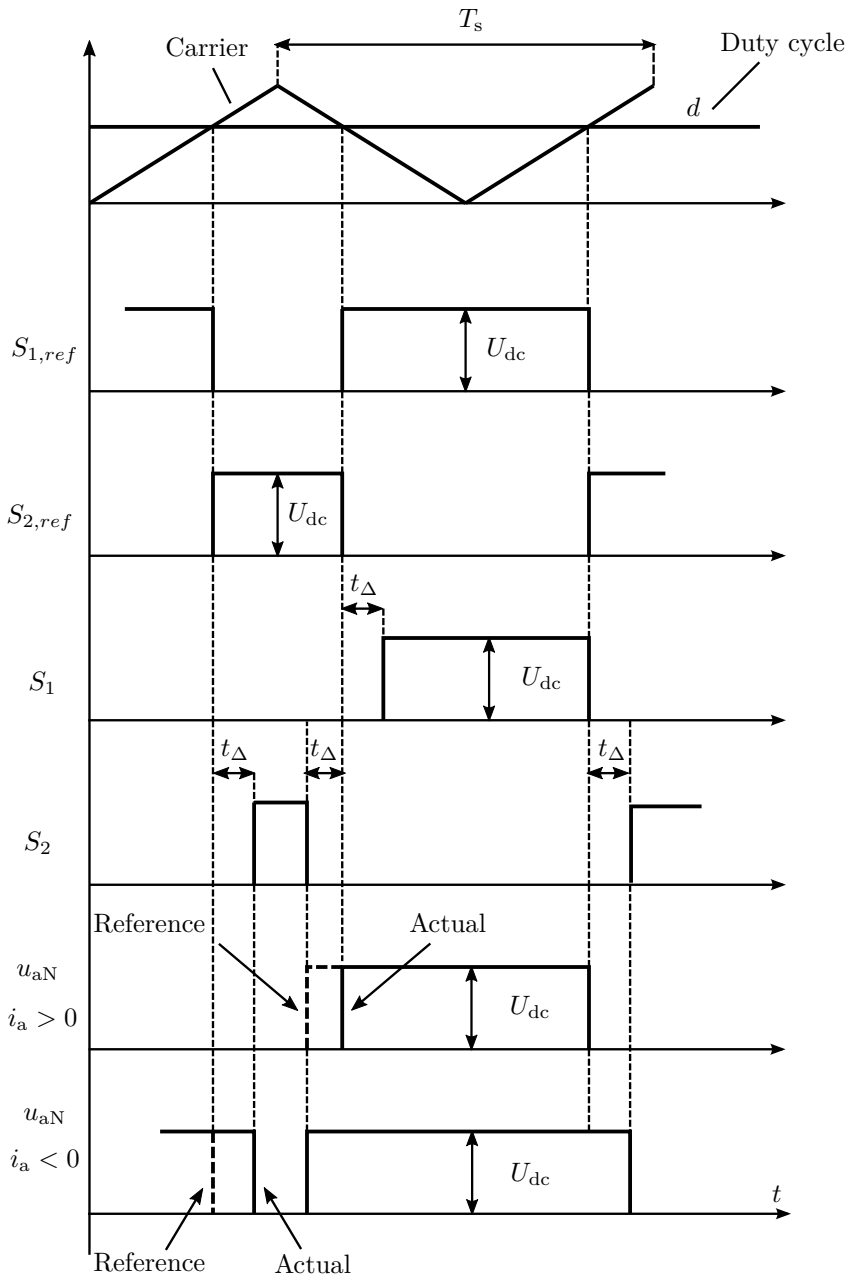

Figure 2.10: The effect of the dead time on the output voltage of the phase a of a three-phase inverter.

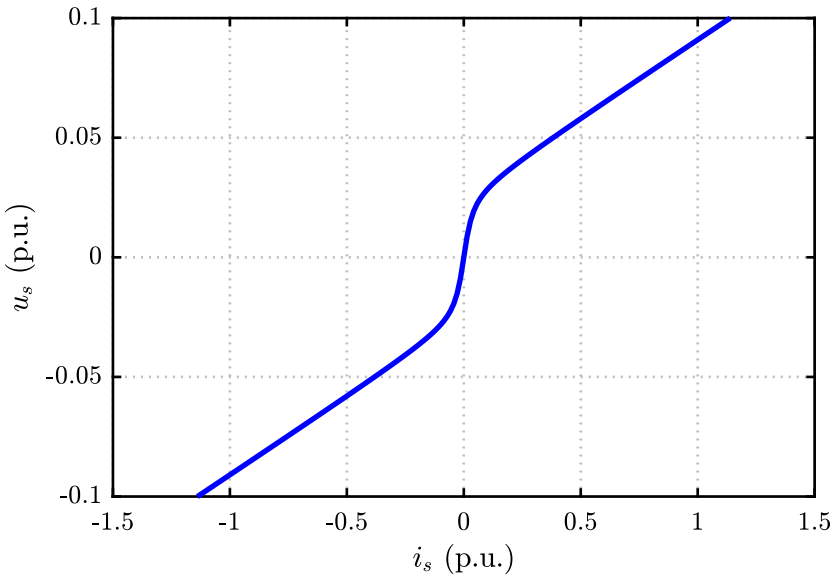

Figure 2.11: Example plot of the inverter non-linearity including the blanking time and voltage drop of the switches.

3 State-of-the-Art Identification Methods

IM parameter identification has been studied widely and numerous methods have been developed during the past three decades. The parameters of the equivalent circuit of the motor have to be estimated in order to tune the controllers. Usually, this procedure should be done on site when the inverter is connected to the motor. This procedure is known as the self-commissioning and done automatically by the controller [10]. One of the first self-commissioning schemes was introduced in [5]. Prior to the self-commissioning of the drive systems, classical tests were used for the parameter identification. Classical identification procedure is mainly based on the DC, no-load and locked-rotor tests as mentioned. The stator resistance is identified via the DC test. In the no-load condition, motor should rotate with the synchronous speed where the rotor current is zero and all the stator current goes through the magnetizing branch. In this way, the magnetizing inductance can be identified [3]. By repeating the no-load test with various current amplitudes, the magnetizing curve is obtained. The locked rotor test is used for the leakage inductance identification, due to the fact that the major part of the current goes to the rotor branch. In this test, the magnetizing branch is omitted. This can be considered as a source of inaccuracy [25]. The effect of the power converters on the estimation is not considered in the classical tests since the tests are implemented without the converters. For this reason, the identified parameters using the classical tests are not directly applicable to the vector control schemes [26]. Besides, the classical tests should be implemented by the operators.

In [27], the classical no-load and locked rotor tests have been utilized with the PWM inverter supply. Identified parameters are equal to those obtained by the sinusoidally-excited no-load and locked-rotor tests since the calculations are based on the fundamental components. In [26], a modified method for the classical tests has been developed. For the locked-rotor test, a configuration has been proposed where two of the three motor terminals are short circuited to each other. Therefore, no torque is produced and the need for locking the rotor is not required. This method is named as the pseudo-locked-rotor test. The proposed modified scheme was aimed to make the classical tests applicable for the self-commissioning procedure.

In [28], a self-commissioning method has been presented. The stator resistance is identified by means of DC current injection where two different currents are used. This method is used to compensate the inverter voltage errors. The stator resistance is obtained by

$$\hat{R}_\mathrm{s} = \frac{\boldsymbol{u}_\mathrm{s2} - \boldsymbol{u}_\mathrm{s1}}{\boldsymbol{i}_\mathrm{s2} - \boldsymbol{i}_\mathrm{s1}} \tag{3.1}$$

where $\boldsymbol{i}_\mathrm{s1}$ and $\boldsymbol{i}_\mathrm{s2}$ are two different injected DC currents and $\boldsymbol{u}_\mathrm{s1}$ and $\boldsymbol{u}_\mathrm{s2}$ are two resulting stator voltages. Using the pulse voltages and measuring the peak value of the resulting currents, the stator transient time constant of the motor is approximated. The stator transient time constant is defined as

$$\sigma\tau_\mathrm{s} = \sigma\frac{L_\mathrm{s}}{R_\mathrm{s}} \tag{3.2}$$

where σL_s is the total leakage inductance and L_s is the stator inductance. In other words, by assuming the equal leakage inductance in the rotor side and stator side, the total leakage inductance in the T model is

$$L_{\mathrm{s}\sigma} = L_{\mathrm{r}\sigma} = \frac{\sigma L_\mathrm{s}}{2}. \tag{3.3}$$

The rotor time constant

$$\tau_\mathrm{r} = \frac{L_\mathrm{r}}{R_\mathrm{r}} \tag{3.4}$$

is determined by injecting a DC current to the motor in order to build up the rotor flux and open circuiting the machine after some seconds by turning off the inverter. The magnetizing inductance is identified using the no-load test. In [29], an estimation scheme has been introduced where different operating conditions are evaluated and motor parameters are defined as a function of the operating points. In addition, the sensitivity of the parameter estimation to the frequency has been analyzed. The commissioning methods in [26–29] cannot be considered as fully-standstill identification schemes since not all of the parameters are identified at standstill.

In [5], one of the first standstill parameter identification schemes has been developed. The leakage inductance is identified by injecting DC voltage to the motor terminals. The rotor time constant is estimated by transient tests avoiding the motor to enter the saturation. In addition, the total inertia of the motor is determined through a test run. In [25], the identification method estimates the stator resistance, stator short-circuit time constant $\tau_\mathrm{s} = L_\mathrm{s}/R_\mathrm{s}$, and rotor time constant τ_r at standstill. The stator short-circuit time constant and rotor time constant are identified using a first order recursive least squares (RLS) estimator where the stator voltage is the input and the stator current is the output of the RLS estimator. The excitation signal for estimating τ_s consist of a DC voltage and a high-frequency disturbance

signal produced by a pseudorandom binary sequence. The DC voltage is fed to the motor to create a steady-state current close to the nominal current. Since τ_{s} is much faster than τ_{r}, the current response is dominated by the fast time constant when the high-frequency disturbance is added. The excitation signal for estimating τ_{r} is a step reversal of the applied voltage in order to reverse the flow of the current. In [30], a standstill identification scheme has been presented where the stator resistance, rotor resistance and rotor time constant are identified. The rotor resistance is estimated by injecting a sinusoidal current superimposed to a DC-bias current along the α-axis and using the phase angle. To evaluate the effect of the eddy currents in the rotor bars on the rotor resistance estimation, several different frequencies are tested. Based on the evaluation, the rotor resistance increases with the frequency. The rotor time constant is approximated when the inverter supplies a DC current to the α-axis and then the stator terminals are shorted by turning on all three upper or lower switches of the inverter. In [7], a parameter identification scheme using the single-phase test has been developed. The equations for calculating the parameters of each model has been presented. The excitation signal is the sinusoidal signal with different frequencies. Phasors are calculated by means of the Fourier transformation. Based on the stator voltage, the stator current, and the frequency, the parameters are estimated for all the models. Moreover, an iterative algorithm has been proposed for calculation of the magnetizing inductance. In [31], an identification scheme has been developed where a sinusoidal test signal along α-axis is used for the excitation. Three test signals are chosen for the estimation procedure. An RLS algorithm is implemented for fitting the data obtained from the tests. In [32], a standstill identification scheme was introduced. The excitation signal consists of an AC current superimposed to a set of DC-bias currents. The AC response of the voltages and currents are used to identify the motor parameters. The DC-bias currents are utilized for creating different operating points. In [33], a method for identification of the rotor resistance and magnetizing inductance of the T model at standstill was proposed. The test signal is a set of low-frequency sinusoidal currents along α-axis as the reference currents. The excitation frequency is the nominal slip frequency. Additionally, the voltage drop caused by the inverter is taken into account by means of a resistance added to the stator resistance in the identification procedure. The main drawback of the identification schemes in [5, 7, 25, 30–33] is that all the motor parameters are considered constant. Therefore, the magnetic saturation characteristic is not taken into consideration.

In [6], a step-by-step self-commissioning scheme has been developed based on [34] and [35]. Different test signals are utilized in the identification procedure. The inverter non-linearity and magnetic saturation of the magnetizing inductance are taken into account. The discrete-time motor model is derived and physical parameters are then achieved by means of the RLS algorithm. Experimental results show some inaccuracies in the magnetizing inductance estimation at low current levels.

In [36], a standstill identification has been proposed where a model reference adaptive system (MRAS) approach is used and a parallel adaptive observer is designed.

During the identification, the rotor flux is estimated. The principle of the identification is based on preventing the occurrence of the saturation in the estimation process. To avoid the motor to enter the saturation, the rotor flux level estimator is used to check the state of the IM to be in the linear region. Although, the identification results are acceptable, the adaptive reference model is needed which increases the complexity of the implementation.

Since the identification of the magnetizing curve is one of the most challenging phases of the estimation procedure, several schemes are available in literature focusing on the magnetizing inductance estimation. In [37], a method has been introduced where a set of fundamental components of the stator voltage are measured in the steady state. A polynomial function is used for modeling the inverse of the magnetizing curve. The coefficients of the saturation characteristic function are estimated by means of experiments. The experiments are carried out in various operating speeds in the field weakening region. The scheme requires the motor to rotate, thus the identification is not at standstill. In addition, the stator voltage measurements are required.

In [38], a method for identification of the magnetizing inductance has been introduced where a broadband excitation signal is used. This signal injects multiple frequencies at the same time. The excitation signal consists of a multiple frequency wave superimposed to a DC current. For the multiple frequency wave, a range of a hundred different frequencies is used. The stator current and voltage are measured in the time domain and then transformed into the frequency domain by means of the discrete Fourier transform (DFT). The coefficients of the motor transfer function are identified by means of a maximum likelihood estimator. In [39], the magnetic saturation characteristic of the induction motor has been evaluated at standstill using a single test. The inverse-Γ model rotor resistance is identified together with the magnetizing inductance. In addition, a single-axis excitation has been proposed where a low-frequency sinusoidal signal is used.

3.1 Single-Axis Sinusoidal Excitation

In [16], an iterative identification method has been presented. Based on the Γ-model, the equations for calculating the magnetizing inductance L_{M}, rotor resistance R_{R} and leakage inductance L_σ are derived. The magnetic saturation characteristic is taken into account. The excitation signal is the sinusoidal current along one axis (e.g., α-axis) as

$$\boldsymbol{i}_{\mathrm{s}} = I_{\mathrm{s}} \sin \omega t. \tag{3.5}$$

Two different frequencies are utilized in order to estimate the parameters. An angular frequency ω_1 is introduced as

$$\omega_1 \approx \frac{1}{8} \frac{R_{\mathrm{R}}}{L_\sigma} \tag{3.6}$$

where the magnetizing current dominates the stator current and the magnetizing inductance identification becomes insensitive against the leakage inductance errors. A higher angular frequency ω_2 is introduced as

$$\omega_2 \approx \frac{1}{2} \frac{R_{\mathrm{R}}}{L_\sigma} \tag{3.7}$$

where the rotor current dominates the stator current. Consequently, estimation of the leakage inductance becomes insensitive against the magnetizing inductance errors. Knowing one of the inductances in a certain operating point, the other inductance and the rotor resistance can be obtained by means of the measured data for the same operating point. In order to create different operating points, a set of current amplitudes I_{s} is chosen within a range of zero to the nominal current of the motor. The sinusoidal currents with two angular frequencies given in (3.6) and (3.7) are fed to the motor and phasors are calculated.

The phasors for the estimation algorithm can be computed in a computationally efficient way using the Goertzel algorithm [40, 41]. The Goertzel algorithm is an efficient implementation of DFT. From the computational perspective, the Goertzel algorithm is more efficient than the fast Fourier transform. The fast Fourier transform computes all N samples of the DFT in order to obtain a high efficiency. Nevertheless, the Goertzel algorithm requires the samples of the DFT over a portion of the frequency range $0 \leq \omega < 2\pi$. Besides, the number of the samples can be increased without an effect on the computation time [41]. The Goertzel algorithm is explained briefly in Appendix A.

The magnetizing voltage is

$$U_{\mathrm{M}} = \sqrt{\left(U_{\mathrm{s}} - R_{\mathrm{s}} I_{\mathrm{s}} \cos \phi_{\mathrm{s}}\right)^2 + \left(R_{\mathrm{s}} I_{\mathrm{s}} \sin \phi_{\mathrm{s}}\right)^2} \tag{3.8}$$

and can be calculated according to Figure 3.1, where U_s is the stator voltage amplitude, and ϕ_s is the phase angle. The phase angle between the stator current and stator flux can be obtained by

$$\delta_\mathrm{s} = \arctan\left(\frac{U_\mathrm{s} - R_\mathrm{s} I_\mathrm{s} \cos\phi_\mathrm{s}}{R_\mathrm{s} I_\mathrm{s} \sin\phi_\mathrm{s}}\right) - \phi_\mathrm{s}. \tag{3.9}$$

The identification algorithm starts with an initial guess for the leakage inductance $L_\sigma(0)$. Based on the Γ-model equivalent circuit, if L_σ is known, the rotor resistance and magnetizing inductance can be obtained by

$$R_\mathrm{R} = \frac{U_\mathrm{M}}{2 I_\mathrm{s} \sin\delta_\mathrm{s}} + \sqrt{\left(\frac{U_\mathrm{M}}{2 I_\mathrm{s} \sin\delta_\mathrm{s}}\right)^2 - \omega^2 L_\sigma^2} \tag{3.10}$$

$$L_\mathrm{M} = \frac{1}{\dfrac{\omega I_\mathrm{s} \cos\delta_\mathrm{s}}{U_\mathrm{M}} - \dfrac{\omega^2 L_\sigma}{R_\mathrm{R}^2 + \omega^2 L_\sigma^2}} \tag{3.11}$$

and if L_M is known, the leakage inductance can be calculated by

$$L_\sigma = \frac{\dfrac{1}{\omega}\left(\dfrac{I_\mathrm{s}}{U_\mathrm{M}} \cos\delta_\mathrm{s} - \dfrac{1}{\omega L_\mathrm{M}}\right)}{\left(\dfrac{I_\mathrm{s}}{U_\mathrm{M}} \sin\delta_\mathrm{s}\right)^2 + \left(\dfrac{1}{\omega L_\mathrm{M}} - \dfrac{I_\mathrm{s}}{U_\mathrm{M}} \cos\delta_\mathrm{s}\right)^2}. \tag{3.12}$$

Using the lower angular frequency test data, L_M is calculated by the expression (3.11). The calculated L_M is inserted into (3.12) and using the higher angular frequency test data, a new value for the leakage inductance is estimated. The new L_σ is updated into (3.10) and (3.11), respectively. Therefore, the new rotor resistance and magnetizing inductance are calculated. The iteration at each operating point continues till the value of L_σ converges to a fixed value which gives the identified parameters at that operating point. Finally, the coefficients of the saturation characteristic in expression (2.33) can be estimated directly by means of the linear least squares (LLS) method. The LLS method for estimating the saturation function coefficients is explained briefly in Appendix B. Figure 3.2 represents the block diagram of the identification method.

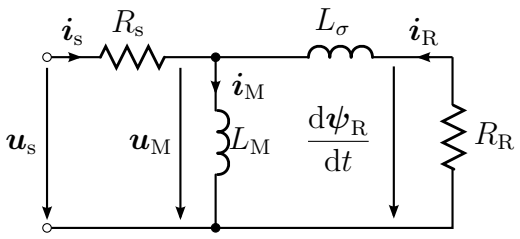

Figure 3.1: Γ equivalent circuit at standstill.

As illustrated, the starting point of the estimation algorithm requires an initial value for the leakage inductance $L_\sigma(0)$. In the beginning of the identification, the leakage inductance is unknown. Therefore, the initial guess of the leakage inductance $L_\sigma(0)$ contains some errors inevitably. Hence, the robustness of the algorithm against the $L_\sigma(0)$ errors should be evaluated. Figure 3.3 illustrates the robustness of the method against the initial guess of the leakage inductance. Initial guess for the leakage inductance can be in the range of zero to approximately five times of the actual L_σ value. In addition, simulations show that the convergence of L_σ occurs quite fast and takes only a few number of iteration cycles (around four cycles).

Figure 3.4 gives the estimation of the magnetizing inductance as a function of the stator flux. It can be seen that the identification of the magnetizing inductance is accurate when there is no saturation. The error between the estimated and real values appear when saturation starts. This phenomenon has been studied thoroughly in [42].

The stator flux is a pulsating waveform in the single-phase sinusoidal excitation, i.e., sinusoidal excitation along one axis. The chord-slope inductance L_M in the single-phase excitation pulsates between a maximum and minimum value as in Figure 3.5. In the three-phase sinusoidal excitation, the stator flux is rotating and constant. Hence, the chord-slope L_M is constant and is equal to the minimum value in the single-phase excitation as in Figure 3.5. Increasing the excitation current amplitude increases the fluctuation in L_M. The error in the magnetizing inductance estimate becomes larger as the saturation level gets higher. Figure 3.6 shows the magnetizing inductance in the single-phase and three-phase excitations, and the estimate of L_M when the motor is highly saturated. Figure 3.7 illustrates the fluctuation of the flux as a function of the magnetizing current in a highly saturated region. The stator flux pulsates between two points, 1 and 2, which is shown with red color. This

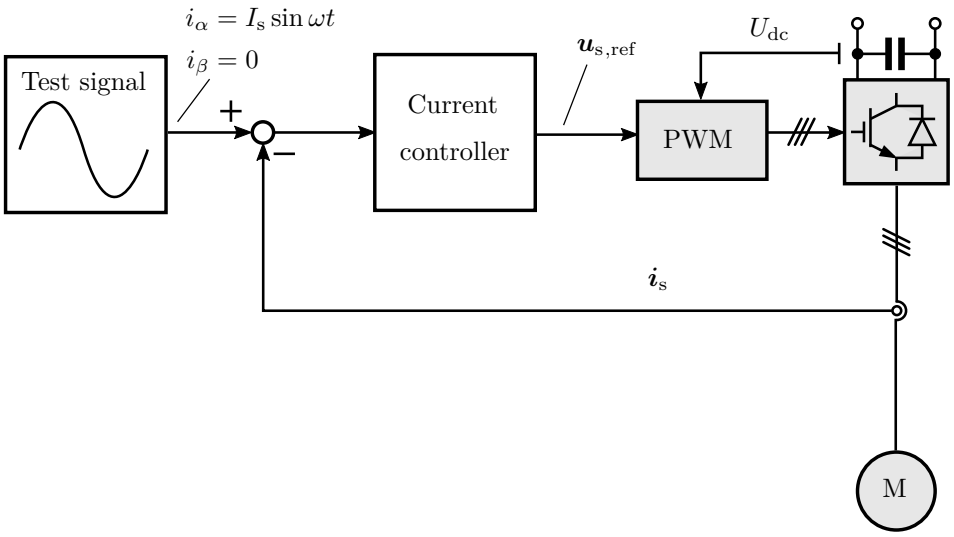

Figure 3.2: Identification set-up for the single-axis sinusoidal excitation.

pulsating area contains the linear region and saturation region. In the linear region, the chord-slope L_{M} and incremental L_{Mi} are equal. In the saturation region, the incremental inductance changes due to the change in the the tangent of the saturation curve. In this region, the higher is the saturation, the higher is the amplitude of the fluctuation of the chord-slope L_{M}. However, the incremental inductance L_{Mi} decreases due to the decrease in the tangent of the saturation curve. The effect of the incremental inductance varies with the excitation current amplitude and the error becomes larger with the rise in the current amplitude.

The leakage inductance and rotor resistance are identified using the single-axis sinusoidal excitation. The estimated leakage inductance is 0.1714 p.u. and the estimated value for the rotor resistance is 0.0395 p.u. The actual values for the leakage inductance and rotor resistance in the simulation model are 0.17 p.u. and 0.040 p.u., respectively. Therefore, the estimation error for the leakage inductance is less than 1% and the estimation error for the rotor resistance is around -1.2%.

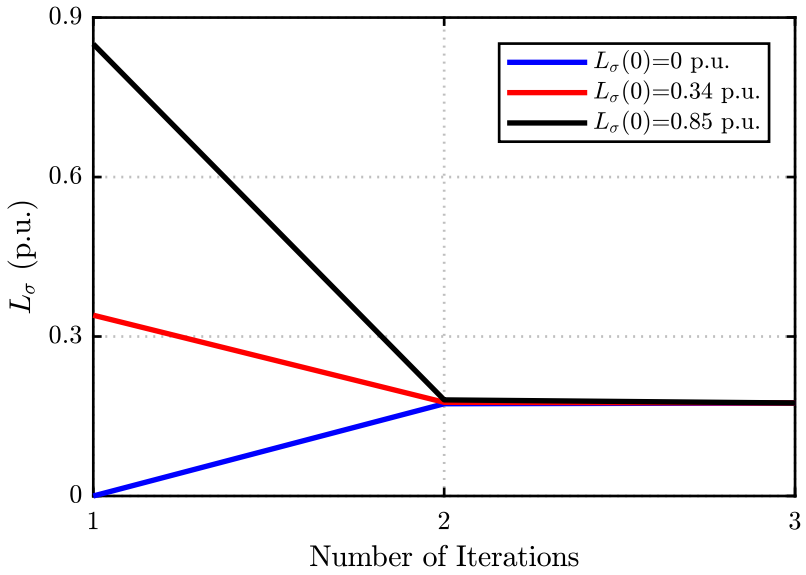

Figure 3.3: Convergence of the leakage inductance as a function of the iteration cycles.

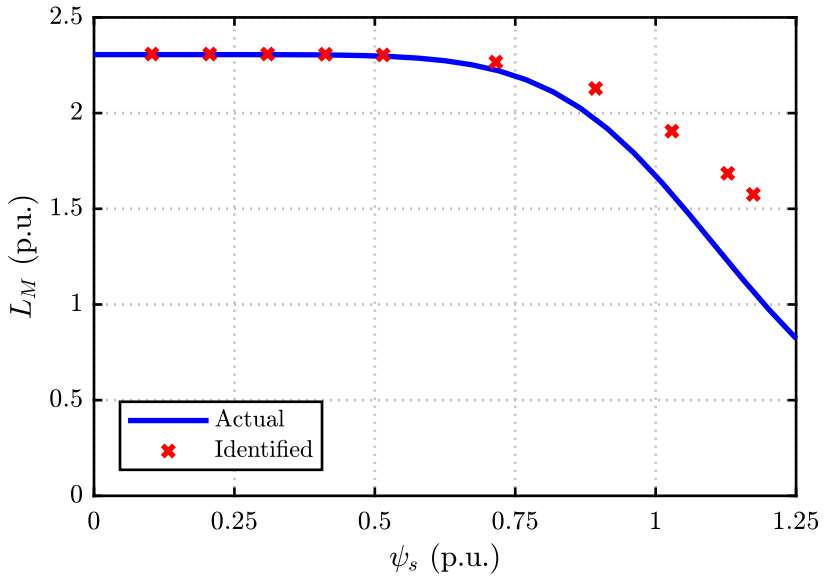

Figure 3.4: Estimation of the magnetizing inductance as a function of the stator flux.

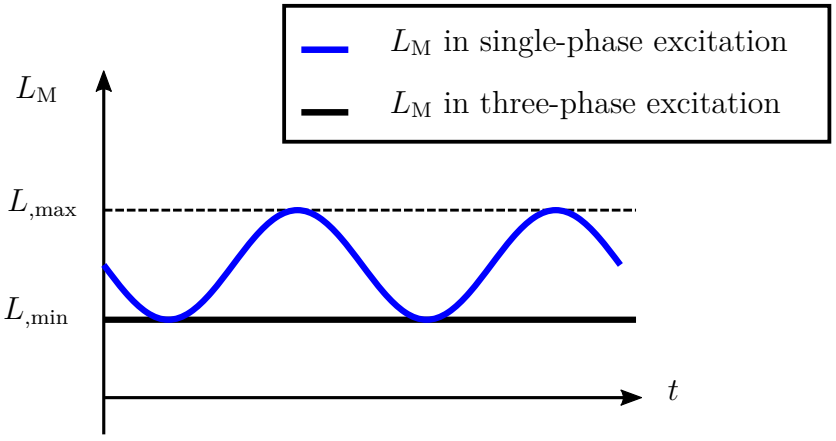

Figure 3.5: Pulsating chord-slope L_{M} in the single-phase excitation and constant chord-slope L_{M} in the three-phase excitation.

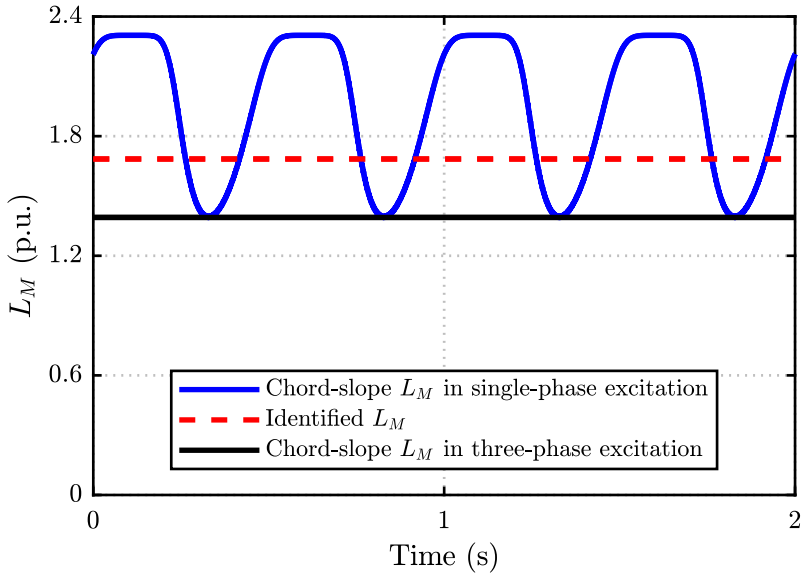

Figure 3.6: Chord-slope magnetizing inductance in the single-phase and three-phase excitations, with its estimated value, when the motor is highly saturated.

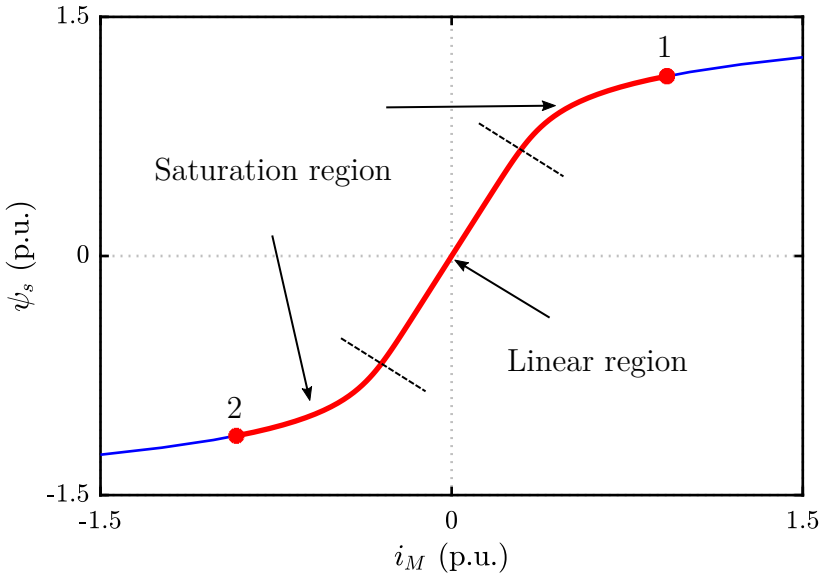

Figure 3.7: Graphical interpretation of the pulsating stator flux as a function of the magnetizing current in the single-phase excitation when the motor is highly saturated.

3.2 Single-Axis Sinusoidal Excitation for the Magnetizing Inductance Identification

In [43], estimation of the magnetizing inductance in the inverse-Γ model has been presented. The test strategy is based on the sinusoidal voltage input on the stator terminals and for this purpose, a sinusoidal current is fed to one axis as introduced in (3.5). The reference voltage is the output of a PI current controller. To achieve the magnetizing curve of the motor, different operating points should be evaluated, thus the discrete-time test current amplitude is

$$i(k+1) = i(k) + \Delta i(k) \tag{3.13}$$

where $\Delta i(k)$ is the current step added to the previous value to produce an increasing current. Figure 3.8 shows the test signal waveform. Prior to the estimation of the magnetizing curve, the stator resistance and the leakage inductance should be estimated. The leakage inductance, which is considered constant, is identified using high-frequency AC tests to neglect the magnetizing branch. The imaginary part of the impedance is used to estimate the leakage inductance. The test frequency for the magnetizing inductance estimation is relatively low and obtained by (3.6). Furthermore, a resonance filter is tuned at the injected frequency to filter out the harmonics and to calculate the phasors. The alternative solution to obtain the phasors is to use the Goertzel algorithm as mentioned before.

Identification procedure is similar to the scheme in [16]. The proposed scheme only identifies the magnetizing inductance. The increase in the test signal amplitude should be sufficiently slow in order to achieve the steady state condition for the curve identification. This duration is not mentioned in the scheme. In addition, obtaining the magnetizing flux for plotting the magnetic curve is implicit and not mentioned.

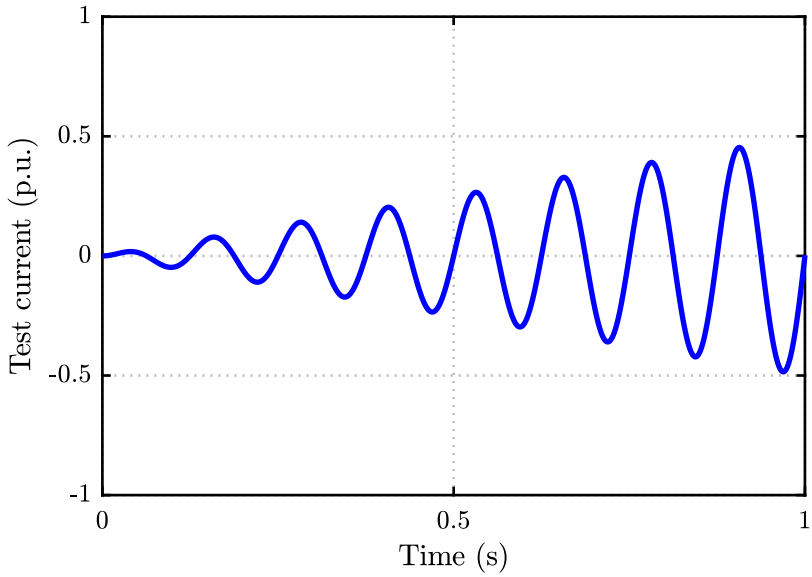

Figure 3.8: Test current for the magnetizing inductance identification.

3.3 Slow-Ramp Excitation for the Magnetizing Inductance Identification

In [44], the magnetizing inductance is estimated using a single test signal at standstill. In the beginning, the inverter non-linear characteristic is identified by means of closed-loop current control. The obtained inverter non-linearity is compensated. The excitation signal for the magnetizing inductance identification is a single-axis slow-ramp voltage where an open current loop is used. The magnetizing flux in the inverse-Γ model of Figure 3.9 can be obtained by

$$\psi'_{\mathrm{M}} = \int_0^t (u_{\mathrm{s}} - R_{\mathrm{s}} i_{\mathrm{s}})\,\mathrm{d}t - L'_\sigma i_{\mathrm{s}} \tag{3.14}$$

and the magnetizing current can be calculated by

$$i'_{\mathrm{M}} = i_{\mathrm{s}} - \frac{u_{\mathrm{s}} - R_{\mathrm{s}} i_{\mathrm{s}} - L'_\sigma \dfrac{\mathrm{d}i_{\mathrm{s}}}{\mathrm{d}t}}{R'_{\mathrm{R}}}. \tag{3.15}$$

The excitation voltage, measured current, estimated magnetizing flux and calculated magnetizing current waveforms are shown in Figure 3.10. The magnetizing inductance L'_{M} can be obtained by

$$L'_{\mathrm{M}} = \frac{\psi'_{\mathrm{M}}}{i'_{\mathrm{M}}}. \tag{3.16}$$

The slow-ramp excitation signal is chosen for two main reasons. Firstly, as can be seen in (3.15), the derivation of the current is sensitive to the rapid change of the stator current. Secondly, the calculation of the magnetizing current in (3.15) is dependent on the rotor resistance. The errors of this parameter affect the calculation. The rotor current is low when the slow-ramp excitation is used, as observed in the simulations. Therefore, the effect of the R'_{R} errors on the estimation of the L'_{M} may not be significant. Generally, it takes about $5\tau_{\mathrm{s}}$ for the current response to reach the steady state condition when the step signal is used. Therefore, the proposed ramp signal duration can be approximately $50\tau_{\mathrm{s}}$. Figure 3.11 shows the estimation

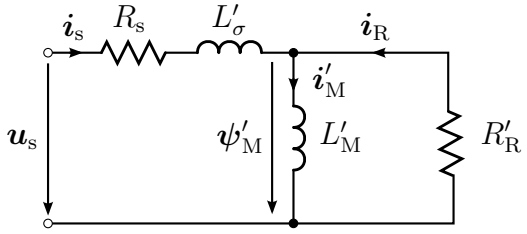

Figure 3.9: Inverse-Γ model at standstill.

of the magnetizing inductance as a function of the magnetizing flux. It should be noticed that for obtaining the magnetizing inductance L'_{M} in Figure 3.11, the same saturation characteristic as the Γ model L_{M} is assumed.

The method does not require any function for modeling the saturation curve and the obtained points in the curve can be given to the controller as a look-up table.

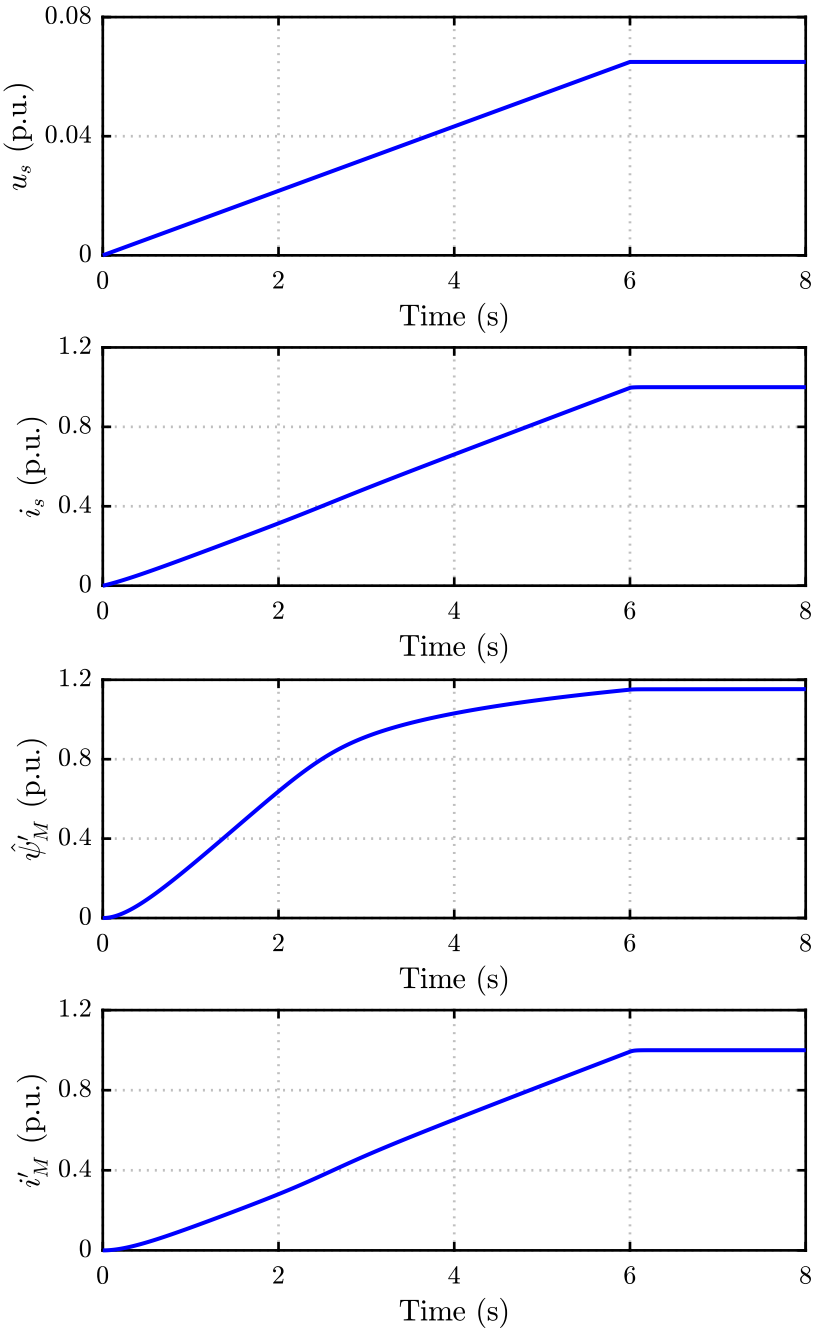

Figure 3.10: Reference stator voltage, measured stator current, estimated magnetizing flux and calculated magnetizing current obtained by the proposed method in [44].

Hence, a fitting algorithm is not needed.

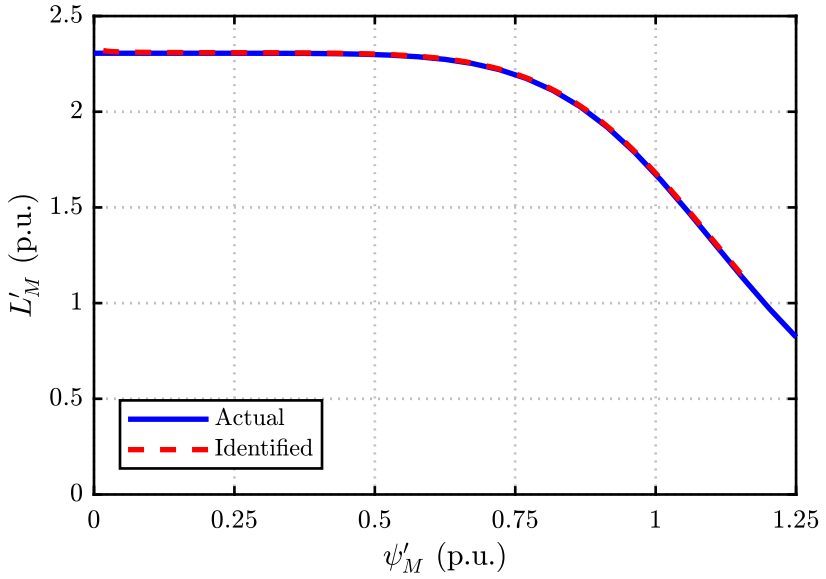

Figure 3.11: Estimation of the magnetizing inductance as a function of the magnetizing flux.

3.4 DC-Decay Test and DC-Biased Sinusoidal Excitation

In [41], a step-by-step method for the inverse-Γ model parameter estimation has been presented. The presented scheme has been later improved in [45]. The identification procedure consists of four steps.

In the first step, R_s is estimated by injecting DC currents. The second phase is to identify the magnetizing inductance using the DC-decay test. Prior to the scheme in [41], the DC-decay test for identification of the synchronous motor parameters at standstill has been introduced, e.g., in [46]. The DC-decay test consists of two steps. In the beginning, a DC current is injected to the motor. This current creates a DC steady-state operating point. The stator flux can be obtained using the voltage model as

$$\int_0^t (u_\mathrm{s} - R_\mathrm{s} i_\mathrm{s}) \mathrm{d}t = \psi_\mathrm{s}(t) - \psi_\mathrm{s}(0) \tag{3.17}$$

where $\psi_\mathrm{s}(0)$ is the stator flux in the DC steady-state condition and $\psi_\mathrm{s}(t)$ is the stator flux at time instant t. In the second step, the stator terminals are short-circuited using a zero voltage vector. In $t(\infty)$, the stator current and stator flux converge to zero and $\psi_\mathrm{s}(t) = 0$. The estimation of the stator flux in (3.17) becomes

$$\lim_{t\to\infty} \int_0^t (u_\mathrm{s} - R_\mathrm{s} i_\mathrm{s}) \mathrm{d}t = -\psi_\mathrm{s}(0). \tag{3.18}$$

The stator flux estimation is triggered when the zero voltage vector is applied and ends when the estimation reaches the steady-state. The stator inductance $L_\mathrm{s}(i_\mathrm{s})$ is calculated using

$$L_\mathrm{s}(i_\mathrm{s,dc}) = -\frac{1}{i_\mathrm{s,dc}} \lim_{t\to\infty} \int_0^t (u_\mathrm{s} - R_\mathrm{s} i_\mathrm{s}) \mathrm{d}t = \frac{\psi_\mathrm{s}(0)}{i_\mathrm{s,dc}} \tag{3.19}$$

where $i_\mathrm{s,dc}$ is the DC current magnitude. It should be noticed that in practice, the integration can be continued till the measured current falls below the sensibility of the A/D converter [45]. Using the DC-decay test, the chord-slope inductance is linked to the stator flux at different operating points. Figure 3.12 shows the identification setup for the magnetizing inductance using the DC-decay test. Figure 3.13 illustrates the stator voltage and stator current waveforms obtained by the DC-decay test for a DC current of 0.2 p.u. Figure 3.14 shows the stator flux and the estimated stator flux obtained by the DC-decay test for a DC current of 0.2 p.u. Figure 3.15 shows the estimation of the magnetizing inductance as a function of the stator flux.

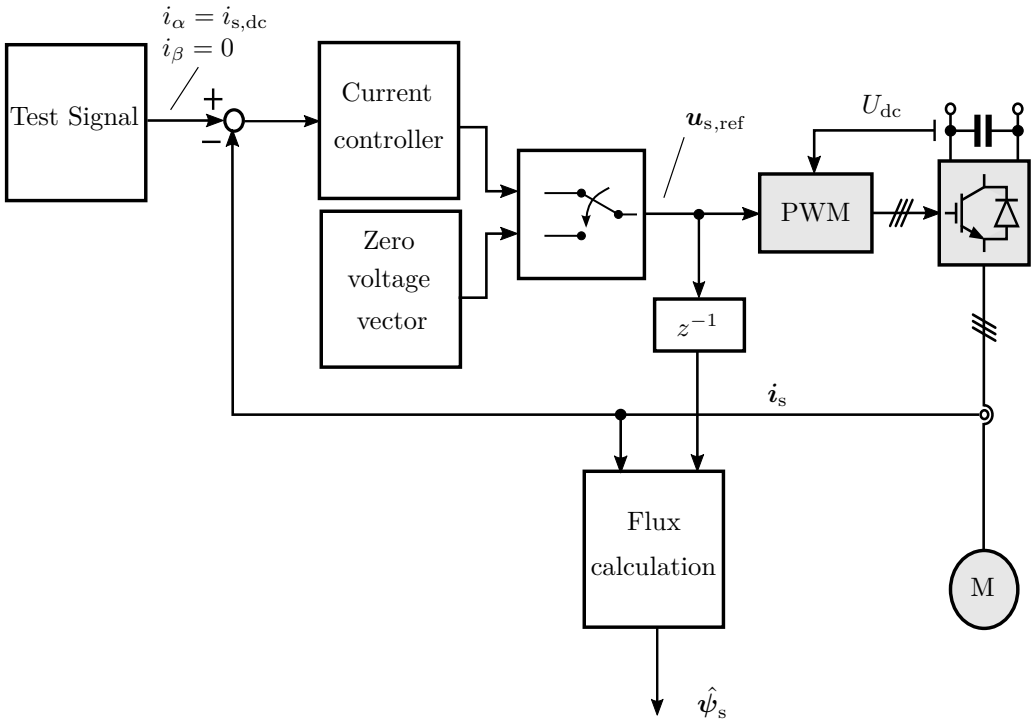

Figure 3.12: Identification setup for the magnetizing inductance using the DC-decay test.

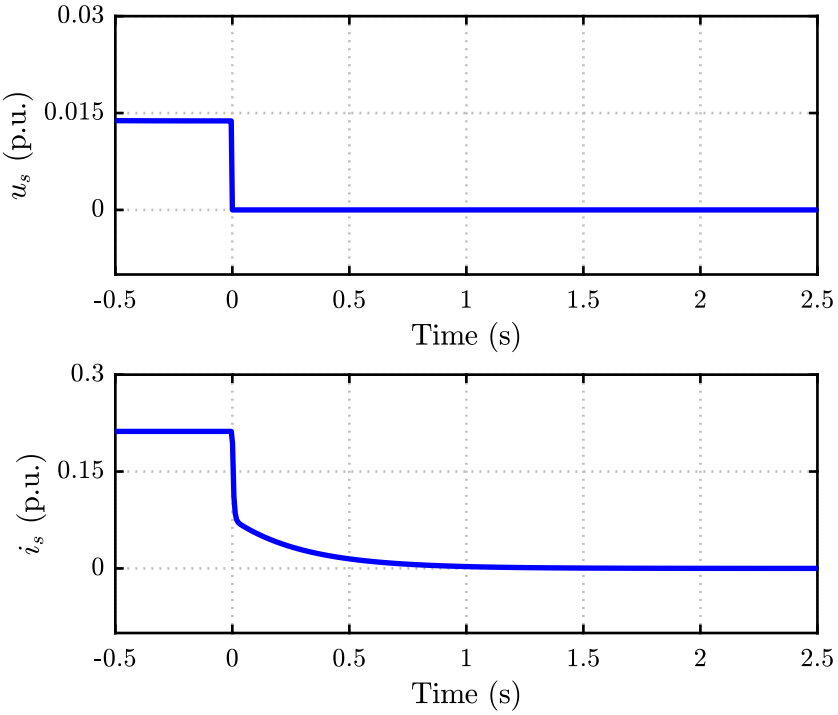

Figure 3.13: Stator voltage and stator current waveforms obtained by the DC-decay test for a DC current of 0.2 p.u.

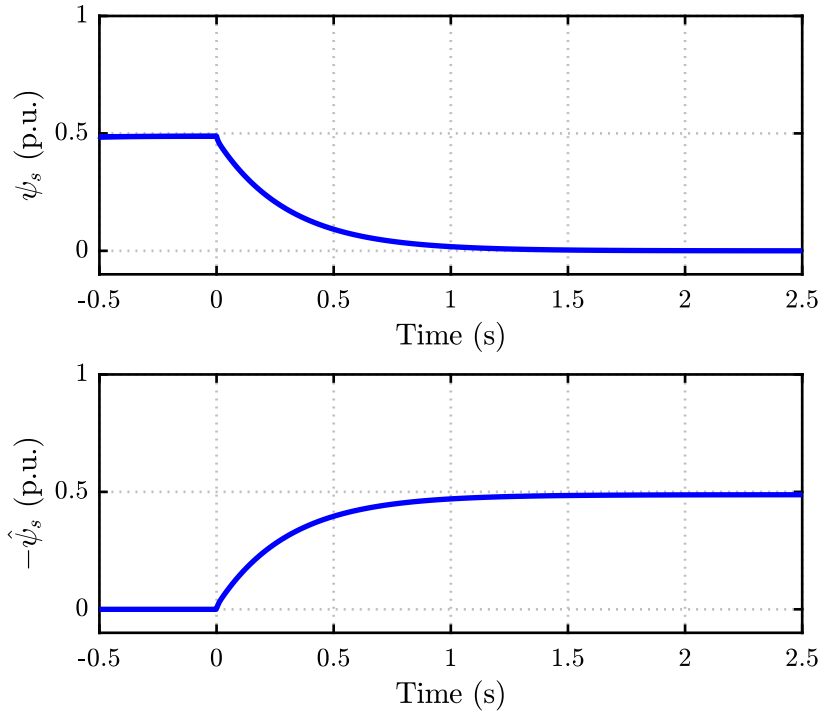

Figure 3.14: Actual and estimated stator flux waveforms obtained by the DC-decay test for a DC current of 0.2 p.u.

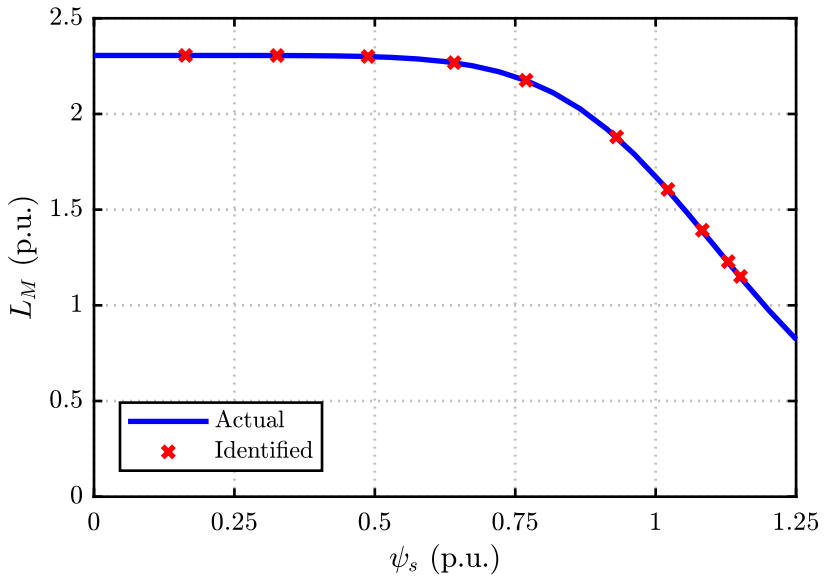

Figure 3.15: Estimation of the magnetizing inductance as a function of the stator flux.

The third step is to estimate the leakage inductance. For this purpose, a high-frequency signal is used. The impedance of the inverse-Γ model is obtained by

$$Z(\mathrm{j}\omega) = R_\mathrm{s} + \mathrm{j}\omega L'_\sigma + \frac{\mathrm{j}\omega L'_\mathrm{M} R'_\mathrm{R}}{\mathrm{j}\omega L'_\mathrm{M} + R'_\mathrm{R}} \tag{3.20}$$

where ω is the angular frequency. When the high-frequency signal is injected to the motor, the impedance of the magnetizing branch becomes much higher than the rotor branch and the magnetizing branch can be omitted. Omitting the magnetizing branch can be explained mathematically as well. In the third term of (3.20), $\mathrm{j}\omega L'_\mathrm{M}$ is much higher as compared to R'_R when the frequency is high. For this reason, R'_R can be omitted from the denominator of the term. Therefore, (3.20) can be approximated to

$$Z(\mathrm{j}\omega) \approx R_\mathrm{s} + \mathrm{j}\omega L'_\sigma + \frac{\mathrm{j}\omega L'_\mathrm{M} R'_\mathrm{R}}{\mathrm{j}\omega L'_\mathrm{M}} \approx R_\mathrm{s} + \mathrm{j}\omega L'_\sigma + R'_\mathrm{R}. \tag{3.21}$$

Figure 3.16 illustrates the approximated inverse-Γ model equivalent circuit at standstill when the high-frequency signal is applied. The high-frequency signal cannot give an acceptable estimation of the rotor resistance. The resistance value increases by the high-frequency signal due to the eddy currents in the rotor bars, leading to fake results [47,48]. Therefore, using this test, only L'_σ will be obtained. The leakage inductance is identified using a DC-biased sinusoidal voltage as

$$\boldsymbol{u}_\mathrm{s} = U_\mathrm{s0} + U_\mathrm{s} \sin \omega t \tag{3.22}$$

where a sinusoidal signal with a small amplitude U_s is superimposed to a set of DC-bias voltages U_s0. This signal produces a sinusoidal current as

$$\boldsymbol{i}_\mathrm{s} = I_\mathrm{s0} + I_\mathrm{s} \sin(\omega t + \phi_\mathrm{s}) \tag{3.23}$$

lagging the voltage by the angle ϕ_s. The DC-bias voltages are chosen to produce the DC currents within the range of zero to the nominal rating of the motor. The frequency for identification of the leakage inductance can be about five times the rated frequency. The incremental inductance is calculated around each operating point. In other words, the leakage inductance is linearized around the operating points.

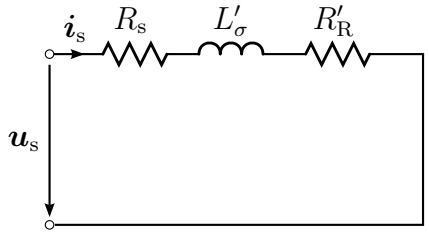

Figure 3.16: Approximate inverse-Γ model at standstill by applying the high-frequency signal.

Using the stator voltage and stator current, the incremental leakage inductance is calculated by

$$L'_\sigma = \frac{\mathrm{Im}\{Z(\mathrm{j}\omega)\}}{\omega} = \frac{1}{\omega}\frac{U_\mathrm{s}}{I_\mathrm{s}}\sin\phi_\mathrm{s} \tag{3.24}$$

where the phasors are obtained by the Goertzel algorithm. Figure 3.17 shows the actual and identified inverse-Γ model leakage inductance L'_σ as a function of the DC-bias current. It should be mentioned that the chord-slope and incremental leakage inductances are equal here since a constant leakage inductance is considered.

As mentioned before, the Γ model is chosen for the identification procedure. The identification scheme estimates the L'_σ. The parameters of the inverse-Γ model can be transformed into those of the Γ model and vice versa by means of the scaling factor [8]. A transformation algorithm for the estimated parameters is explained here. First, the chord-slope magnetizing inductance L_M is identified by the DC-decay test. The exponent S can be fixed and the coefficients c_0 and c_s in (2.33) are estimated directly by means of the LLS method. In the second step, the inverse-Γ leakage inductance L'_σ is identified with a set of DC voltages superimposed to a high-frequency AC signal. According to Figure 3.1, the DC component and a part of the sinusoidal current flow through the magnetizing branch. This sinusoidal current component sees the incremental inductance L_Mi, whose value can be obtained by inserting the estimated c_0 and c_s into the expression (2.35). Therefore, the scaling factor γ_3 as

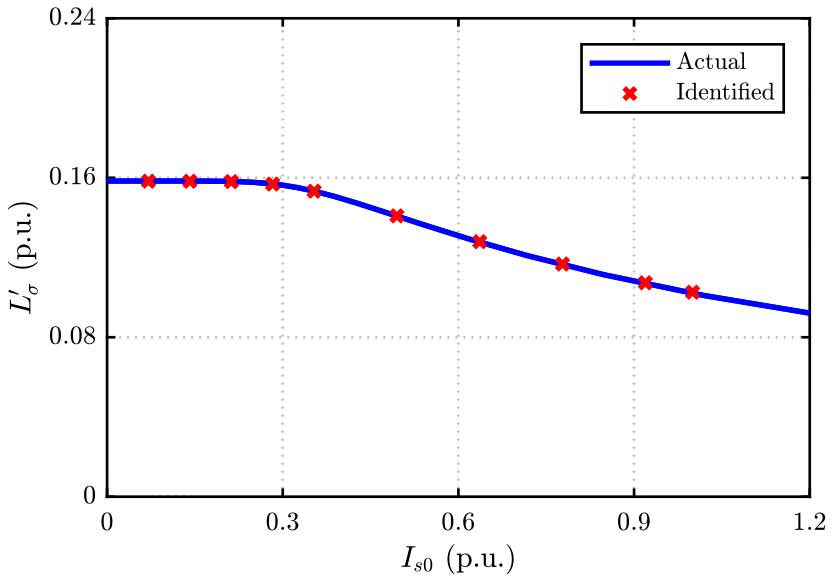

Figure 3.17: Estimation of the inverse-Γ model leakage inductance L'_σ as a function of the DC-bias current.

well as the transformed L_σ and R_R can be obtained as

$$\gamma_3 = \frac{L_\mathrm{Mi} - L'_\sigma}{L_\mathrm{Mi}} \tag{3.25a}$$

$$L_\sigma = \frac{L'_\sigma}{\gamma_3} \tag{3.25b}$$

$$R_\mathrm{R} = \frac{R'_\mathrm{R}}{\gamma_3^2}. \tag{3.25c}$$

Using (3.25), L'_σ of Figure 3.17 can be transformed into L_σ. Figure 3.18 shows the transformed L_σ as a function of the DC-bias current using the transformation algorithm.

In the final step of the identification procedure, the rotor resistance is identified using a DC-biased sinusoidal voltage with a single DC offset. This DC offset should be sufficiently high to move the AC voltage from the near-zero region due to the inverter nonlinearity. The frequency for estimating the rotor resistance can be within a range from zero to the nominal slip frequency. This excitation signal for identification of the rotor resistance has been introduced, e.g., in [30]. The rotor resistance can be derived from (3.20) by means of algebraic simplification as

$$R'_\mathrm{R} = \frac{(\mathrm{j}\omega L'_\mathrm{M})\left[(R_\mathrm{s} + \mathrm{j}\omega L'_\sigma) - Z(\mathrm{j}\omega)\right]}{Z(\mathrm{j}\omega) - (R_\mathrm{s} + \mathrm{j}\omega L'_\sigma + \mathrm{j}\omega L'_\mathrm{M})}. \tag{3.26}$$

The imaginary part of (3.26) is zero and thus, (3.26) becomes

$$R'_\mathrm{R} = \frac{U_\mathrm{s}^2 + R_\mathrm{s}^2 I_\mathrm{s}^2 + \omega^2 {L'_\sigma}^2 I_\mathrm{s}^2}{U_\mathrm{s} I_\mathrm{s} \cos\phi_\mathrm{s} - R_\mathrm{s} I_\mathrm{s}^2} - \frac{2U_\mathrm{s}(R_\mathrm{s} I_\mathrm{s} \cos\phi_\mathrm{s} + \omega L'_\sigma I_\mathrm{s} \sin\phi_\mathrm{s})}{U_\mathrm{s} I_\mathrm{s} \cos\phi_\mathrm{s} - R_\mathrm{s} I_\mathrm{s}^2}. \tag{3.27}$$

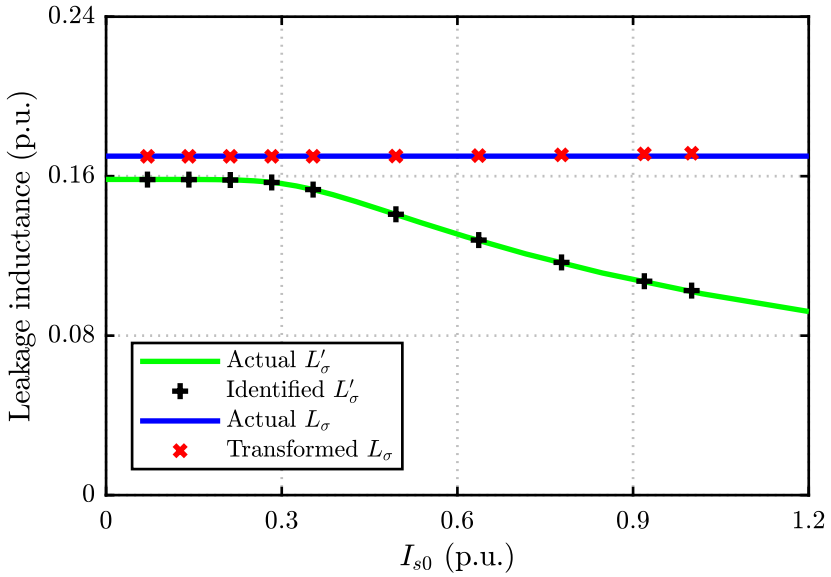

Figure 3.18: Estimated L'_σ and transformed L_σ as a function of the DC-bias current.

The rotor resistance can be calculated using an alternative algorithm. Figure 3.19 shows the inverse-Γ equivalent circuit at standstill. The equivalent impedance of the parallel branches is

$$Z_{\mathrm{par}} = R_{\mathrm{par}} + \mathrm{j}X_{\mathrm{par}} \tag{3.28}$$

where R_{par} and X_{par} can be calculated from the total impedance $Z(\mathrm{j}\omega)$ and using the phase angle ϕ_{s} as

$$R_{\mathrm{par}} = Z(\mathrm{j}\omega)\cos(\phi_{\mathrm{s}}) - R_{\mathrm{s}} \tag{3.29a}$$
$$X_{\mathrm{par}} = Z(\mathrm{j}\omega)\sin(\phi_{\mathrm{s}}) - \omega L'_{\sigma}. \tag{3.29b}$$

Using the imaginary and real parts of the impedance obtained by (3.29) the rotor resistance is calculated by [43]

$$R'_{\mathrm{R}} = \frac{R_{\mathrm{par}}^2 + X_{\mathrm{par}}^2}{R_{\mathrm{par}}}. \tag{3.30}$$

The estimated value for the rotor resistance is 0.404 p.u. Therefore, the estimation error is approximately -1%. In the rotor resistance estimation procedure, the inverse-Γ rotor resistance is identified first. Afterwards, using the transformation algorithm, the transformed R_{R} is obtained.

It is worth mentioning that all identification schemes introduced in Section 3 use inverse-Γ model or T model except the schemes in [7] and [16]. Furthermore, the identification scheme in [7] estimates the parameters of all the three motor models.

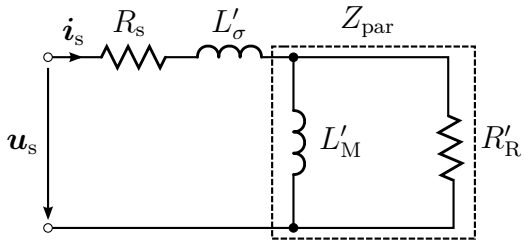

Figure 3.19: Inverse-Γ equivalent circuit at standstill. Z_{par} is the equivalent impedance of the parallel branches.

4 Results

In this thesis, the properties of the identification schemes in [16] and [41] is studied. These two methods are chosen for the comparison, since they are easily applicable and well-known both in academia and industry. Identification methods in [16] and [41] have been implemented in Section 3.1 and Section 3.4, respectively. The main contribution of this thesis is the evaluation of the sensitivity of the methods to the stator resistance and stator voltage errors. In the identification procedure, the stator voltage is reconstructed by means of the DC-link voltage and switching duty cycles. Thus, the voltage distortion caused by the inverter produces an error in the stator voltage. Furthermore, the value of the stator resistance is not perfectly known, even if it is typically measured using the DC-injection test as the first stage of the self-commissioning procedure. Simulation results using a 2.2-kW induction motor which is introduced in Section 2.6 are presented in this section.

4.1 Sensitivity to the Stator Resistance Errors

The sensitivity of the identification methods to the stator resistance errors is evaluated. The evaluation is based on considering two different estimation errors. The estimation errors are as $\hat{R}_\mathrm{s} = 0.9R_\mathrm{s}$ and $\hat{R}_\mathrm{s} = 1.1R_\mathrm{s}$, where $\hat{R}_\mathrm{s}$ is the resistance estimate.

4.1.1 Magnetizing Inductance

Figure 4.1 and Figure 4.2 show the identification results of the magnetizing inductance including the stator resistance estimation errors using the method in [16] and [41], respectively. The estimation error using the method in [41] is lower. Furthermore, Figure 4.1 illustrates that when $\hat{R}_\mathrm{s} = 1.1R_\mathrm{s}$, the estimated L_M is lower than the actual value and when $\hat{R}_\mathrm{s} = 0.9R_\mathrm{s}$, the estimated L_M is higher than the actual value. Figure 4.2 shows the opposite trend for the method in [41]. This phenomenon can be explained by means of the equations used in [16].

Firstly, the expression (3.11) can be written in a simpler way as

$$L_{\mathrm{M}} = \frac{1}{A - B} \tag{4.1}$$

where parameters A and B are defined as

$$A = \frac{\omega I_{\mathrm{s}} \cos \delta_{\mathrm{s}}}{U_{\mathrm{M}}} \tag{4.2a}$$

$$B = \frac{\omega^2 L_\sigma}{R_{\mathrm{R}}^2 + \omega^2 L_\sigma^2}. \tag{4.2b}$$

In a certain operating point and according to (3.8), when $\hat{R}_{\mathrm{s}} = 1.1R_{\mathrm{s}}$, the magnetizing voltage U_{M} decreases compared to the case where $\hat{R}_{\mathrm{s}} = R_{\mathrm{s}}$. In addition, the angle between the stator flux and stator current δ_{s} in (3.9) decreases. Furthermore, R_{R} estimate in (3.10) becomes larger. As a result, in (4.2), A rises and B reduces. The denominator in (4.1) increases while the numerator is constant. Thus, when $\hat{R}_{\mathrm{s}} = 1.1R_{\mathrm{s}}$, the magnetizing inductance estimate is lower as compared to the case where $\hat{R}_{\mathrm{s}} = R_{\mathrm{s}}$. Using a similar manner, it can be proven that when $\hat{R}_{\mathrm{s}} = 0.9R_{\mathrm{s}}$, the magnetizing inductance estimate is larger as compared to the case where $\hat{R}_{\mathrm{s}} = R_{\mathrm{s}}$.

4.1.2 Leakage Inductance

The leakage inductance is estimated using the method in [16] and [41]. The estimation error for the both methods is around 1%. Hence, the both methods estimate the leakage inductance accurately in an ideal condition. Figure 4.3 illustrates the estimation errors of L_σ using the method in [41]. The error rises with the increase in the DC-bias current. The estimation of the L_σ using the method in [16] shows low errors as well. The error is around 6% when $\hat{R}_{\mathrm{s}} = 1.1R_{\mathrm{s}}$ and is negligible when $\hat{R}_{\mathrm{s}} = 0.9R_{\mathrm{s}}$. It can be concluded that the estimation errors of the leakage inductance L_σ are low in both schemes.

4.1.3 Rotor Resistance

The rotor resistance is estimated using the method in [16] and [41]. In an ideal condition, the both schemes show a high accuracy and the estimation error is around 1% for both methods. By adding the stator resistance errors, the estimated rotor resistance using the method in [16] has an error around 12% when $\hat{R}_{\mathrm{s}} = 1.1R_{\mathrm{s}}$ and around 3% when $\hat{R}_{\mathrm{s}} = 0.9R_{\mathrm{s}}$. The estimation error using the scheme in [41] varies when different DC-bias currents are used. Simulations show lower errors when the DC offset current of around 0.5 p.u. is used.

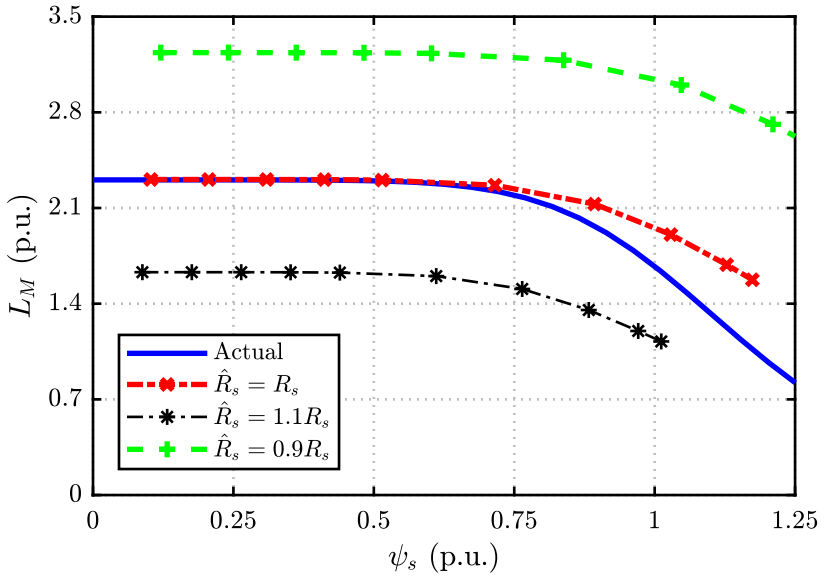

Figure 4.1: Simulation results of L_{M} identification as a function of the stator flux including R_{s} errors using the method in [16].

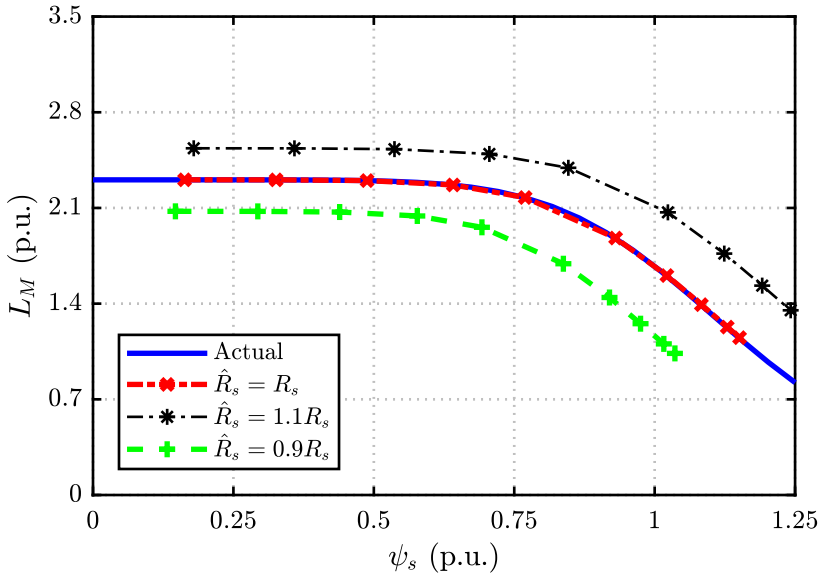

Figure 4.2: Simulation results of L_{M} identification as a function of the stator flux including R_{s} errors using the method in [41].

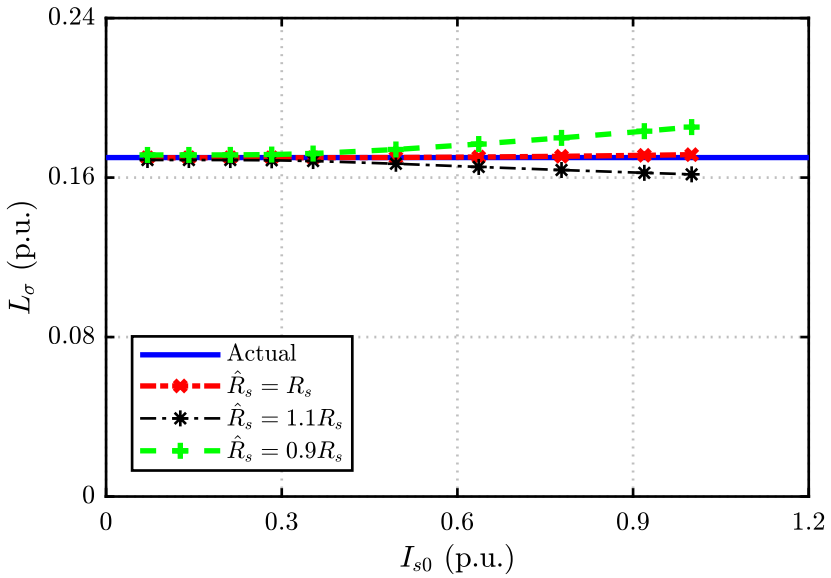

Figure 4.3: Simulation results of L_σ identification as a function of the DC offset current including R_s errors using the method in [41].

4.2 Sensitivity to the Stator Voltage Errors

The sensitivity of the identification methods to the stator voltage errors is evaluated. In this evaluation, the actual stator voltage u_{sa} for the phase a is defined according to (and similarly for other phases)

$$u_{\mathrm{sa}} = u_{\mathrm{a,ref}} - u_{\mathrm{err}}\,\mathrm{sign}(i_{\mathrm{a}}) \tag{4.3}$$

where $u_{\mathrm{a,ref}}$ is the reference phase voltage and u_{err} is the constant voltage error. The considered values for the voltage error u_{err} are 0.0006 p.u. (0.2 V) and 0.0012 p.u. (0.4 V). An accurate stator resistance estimate, $\hat{R}_{\mathrm{s}} = R_{\mathrm{s}}$, is assumed.

4.2.1 Magnetizing Inductance

Figure 4.4 and Figure 4.5 show the sensitivity of the methods in [16] and [41] to the stator voltage errors, respectively. The results illustrate that both method are very sensitive to the stator voltage errors.

4.2.2 Leakage Inductance

In the presence of the inverter voltage errors, the estimation errors of L_σ using the method in [16] is quite low and negligible. Figure 4.6 illustrates the estimated L_σ using the scheme in [41]. In this case, the method in [16] is robust against the inverter voltage errors. It can be concluded from (3.25) that in the presence of the voltage errors, the estimation errors in L_σ using the scheme in [41] is caused by the magnetizing inductance errors. This is due to the fact that the estimated inverse-Γ leakage inductance L'_σ is robust against the stator voltage errors. Figure 4.7 illustrates the robustness of the estimated L'_σ against the stator voltage errors.

4.2.3 Rotor Resistance

In the case of voltage error effects on the estimation of R_{R}, the method in [16] is relatively robust. This error is low as compared to the error in case of the method in [41]. The estimation error is around 2% when $u_{\mathrm{err}} = 0.0006$ p.u. and around 7% when $u_{\mathrm{err}} = 0.0012$ p.u. The estimation error using the scheme in [41] varies when different DC offset currents are used. Simulations show lower errors when the DC offset current of around 0.5 p.u. is used. Figure 4.8 shows the estimation of the rotor resistance as a function of the DC offset current using the method in [41] in the presence of the stator voltage errors..

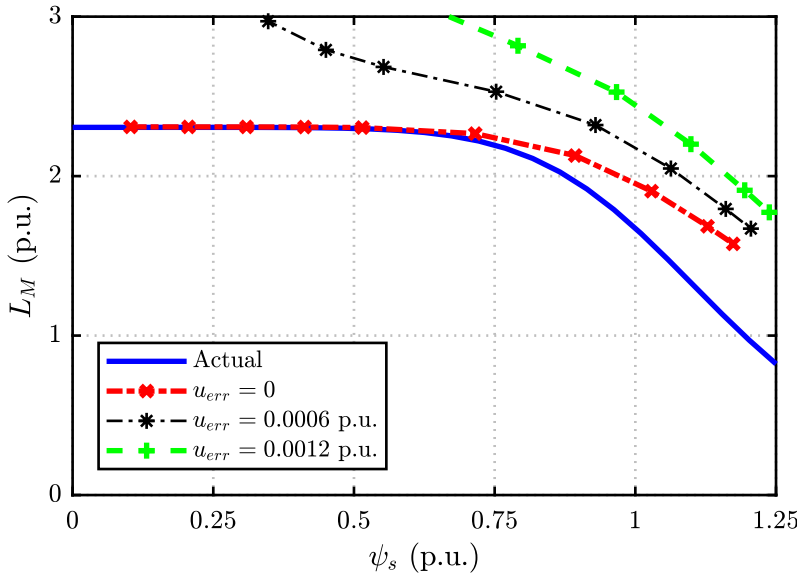

Figure 4.4: Simulation results of L_{M} identification as a function of the stator flux including the stator voltage errors using the method in [16].

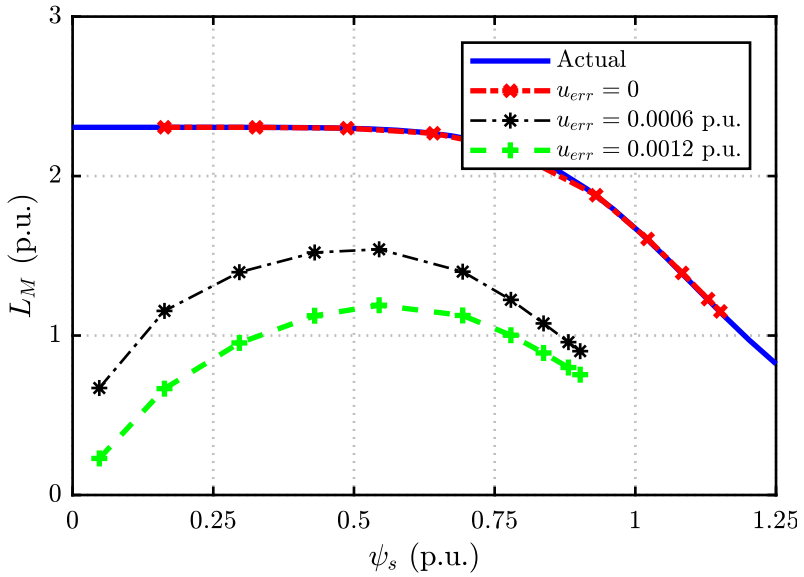

Figure 4.5: Simulation results of L_{M} identification as a function of the stator flux including the stator voltage errors using the method in [41].

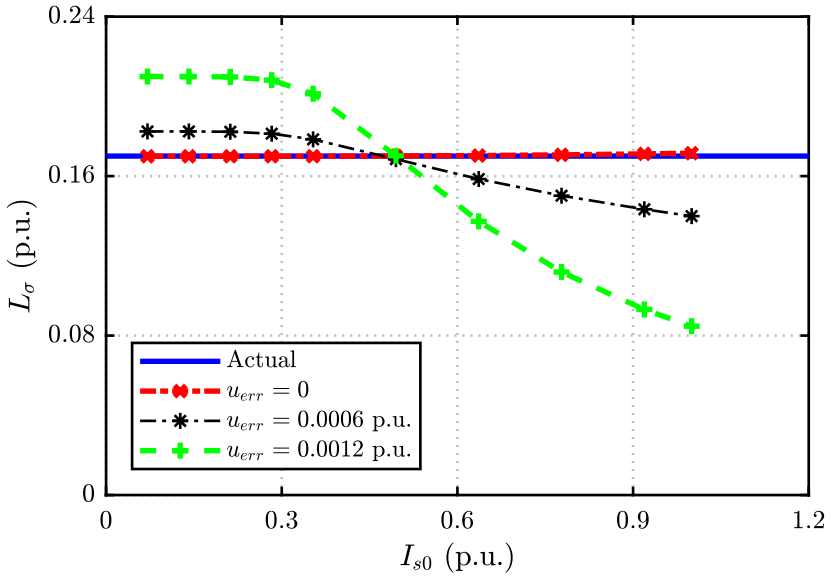

Figure 4.6: Simulation results of L_σ identification as a function of the DC offset current including the stator voltage errors using the method in [41].

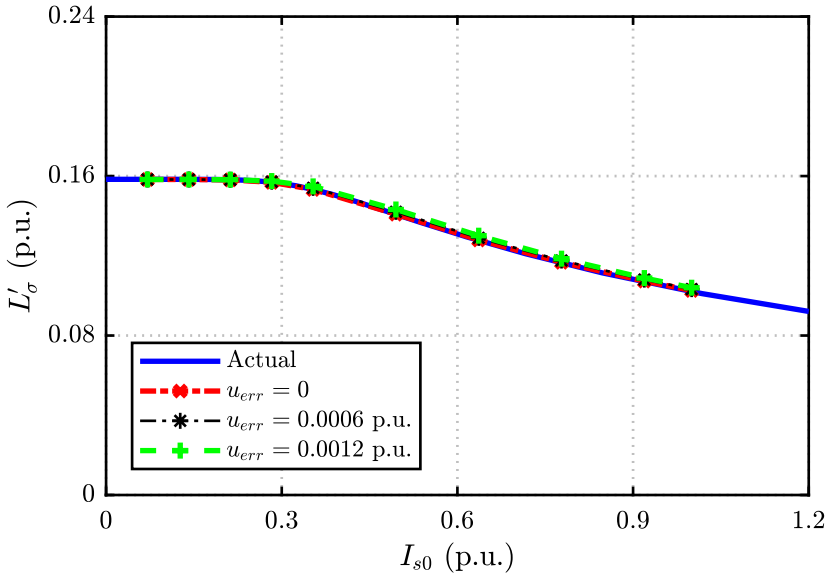

Figure 4.7: Simulation results of L'_σ identification as a function of the DC offset current including the stator voltage errors using the method in [41].

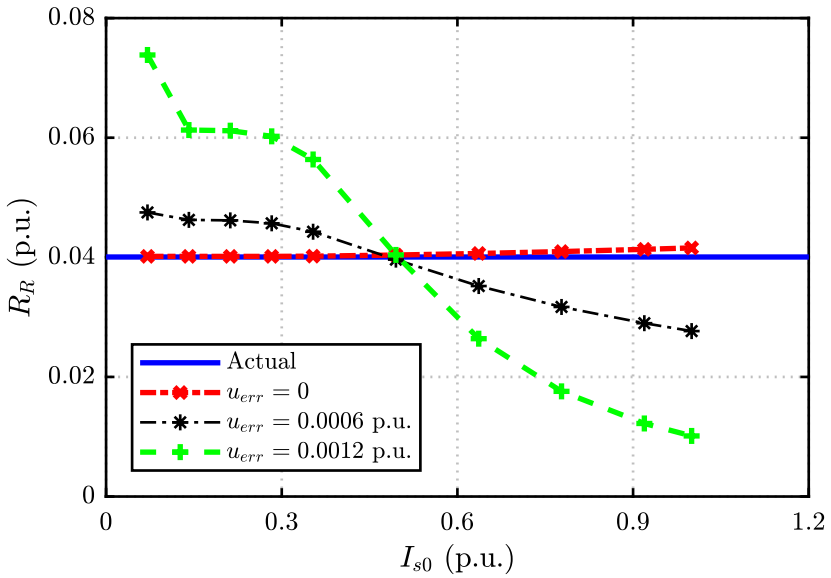

Figure 4.8: Simulation results of R_{R} identification as a function of the DC offset current including the stator voltage errors using the method in [41].

5 Conclusions

In this thesis, the standstill parameter identification methods for the IMs have been studied. The dynamic models of the motors were introduced and the flux and voltage equations for each of the models were presented. The saturation characteristic of the magnetizing inductance has been taken into account. A rational function was used to model the magnetizing inductance as a function of the stator flux.

Numerous methods for IM parameter identification have been developed and several schemes are available in literature. Thus, a literature review for the evaluation of the excitation signals, properties, applicability and drawbacks of the existing methods were conducted. Two different standstill identification schemes were chosen for a detailed comparison. The identification schemes were first implemented in an ideal condition. Thereafter, the sensitivity of the parameter estimation to the stator resistance errors and stator voltage errors was studied. Additionally, the simulation results using a 2.2-kW IM were presented.

An iterative identification scheme at standstill for the Γ model parameters is introduced in the first method. A step-by-step identification scheme for the inverse-Γ model parameter estimation is presented in the second method. For an appropriate comparison, the same motor model was used for both schemes. Thus, the dynamic Γ model at standstill was used as reference. Hence, a transformation method for the estimated parameters of the inverse-Γ model into those of the Γ model has been presented and explained.

The first method uses the single-axis sinusoidal signal as the excitation signal where two angular frequencies are assumed. A low frequency is considered for the estimation of the magnetizing inductance and a comparatively higher frequency is used for the estimation of the leakage inductance. The second method utilizes the DC-decay test for the estimation of the magnetizing inductance. The leakage inductance is identified using DC-biased high-frequency sinusoidal excitation signals. The DC offset currents are chosen to cover a range of zero to the nominal current of the motor. The rotor resistance is identified using a DC-biased sinusoidal voltage. The frequency for the rotor resistance estimation should be sufficiently low due to the eddy currents in the rotor bars.

The properties of the two standstill identification methods were compared. The estimation of the magnetizing inductance becomes inaccurate in the saturated region in the case of the single-axis sinusoidal test signal due to the incremental inductance effect. On the contrary, the DC-decay test is a more suitable method for the magnetizing inductance identification. In addition, the DC-decay test is more robust against the stator resistance errors in case of the magnetizing inductance estimation as compared to the single-axis sinusoidal excitation. The estimation errors of the leakage inductance are low in both methods when the stator resistance errors are taken into account. Both methods are highly sensitive to the inverter voltage errors in the case of the magnetizing inductance estimation. However, the first method can tolerate these errors better in the case of the leakage inductance and rotor resistance identification. The estimation accuracy of the rotor resistance using the DC-biased excitation, in the presence of errors, including the stator resistance errors and voltage errors, depends on the DC offset current.

The future work can be the inclusion of the saturation characteristics of the leakage inductance in order to check the behaviour of L_σ during the identification. The saturation of L_σ may occur when the single-axis sinusoidal excitation is used. Moreover, the motor model can be improved by considering the deep-bar effect to evaluate the rotor resistance estimation dependencies on the frequency. However, these improvements will increase the number of the unknown parameters leading to a more complicated self-commissioning procedure.

References

[1] P. C. Sen, *Principles of electric machines and power electronics*. John Wiley & Sons, 2007.

[2] H. A. Toliyat, E. Levi, and M. Raina, "A review of rfo induction motor parameter estimation techniques," *IEEE Transactions on Energy Conversion*, vol. 18, no. 2, pp. 271–283, June 2003.

[3] M. Ranta, *Dynamic induction machine models including magnetic saturation and iron losses*, ser. Doctoral dissertation. Aalto University, 2013.

[4] D. P. Marčetić, I. R. Krčmar, M. A. Gecić, and P. R. Matić, "Discrete rotor flux and speed estimators for high-speed shaft-sensorless im drives," *IEEE Transactions on Industrial Electronics*, vol. 61, no. 6, pp. 3099–3108, June 2014.

[5] H. Schierling, "Self-commissioning-a novel feature of modern inverter-fed induction motor drives," in *Third International Conference on Power Electronics and Variable-Speed Drives*, Jul 1988, pp. 287–290.

[6] M. Ruff, A. Bunte, and H. Grotstollen, "A new self-commissioning scheme for an asynchronous motor drive system," in *Proceedings of 1994 IEEE Industry Applications Society Annual Meeting*, Oct 1994, pp. 616–623 vol.1.

[7] A. Gastli, "Identification of induction motor equivalent circuit parameters using the single-phase test," *IEEE Transactions on Energy Conversion*, vol. 14, no. 1, pp. 51–56, Mar 1999.

[8] G. R. Slemon, "Modelling of induction machines for electric drives," *IEEE Transactions on Industry Applications*, vol. 25, no. 6, pp. 1126–1131, Nov 1989.

[9] Z. Qu, M. Ranta, M. Hinkkanen, and J. Luomi, "Loss-minimizing flux level control of induction motor drives," *IEEE Transactions on Industry Applications*, vol. 48, no. 3, pp. 952–961, May 2012.

[10] E. Levi, M. Sokola, and S. N. Vukosavic, "A method for magnetizing curve identification in rotor flux oriented induction machines," *IEEE Transactions on Energy Conversion*, vol. 15, no. 2, pp. 157–162, Jun 2000.

[11] T. Tuovinen, M. Hinkkanen, and J. Luomi, "Modeling of saturation due to main and leakage flux interaction in induction machines," *IEEE Transactions on Industry Applications*, vol. 46, no. 3, pp. 937–945, May 2010.

[12] R. J. Kerkman, "Steady-state and transient analyses of an induction machine with saturation of the magnetizing branch," *IEEE Transactions on Industry Applications*, vol. IA-21, no. 1, pp. 226–234, Jan 1985.

[13] P. J. Coussens, A. P. V. den Bossche, and J. A. Melkebeek, "Parameter estimation for induction motor field oriented control using a non-linear motor model," in *Fifth International Conference on Power Electronics and Variable-Speed Drives*, Oct 1994, pp. 198–203.

[14] H. C. J. de Jong, "Saturation in electrical machines," in *Proceeding of international conference on electrical machines*, vol. 3, Athens, Greece, Sept 1980, pp. 1545–1552.

[15] S. N. Vukosavic and E. Levi, "Robust dsp-based efficiency optimization of a variable speed induction motor drive," *IEEE Transactions on Industrial Electronics*, vol. 50, no. 3, pp. 560–570, June 2003.

[16] N. R. Klaes, "Parameter identification of an induction machine with regard to dependencies on saturation," *IEEE Transactions on Industry Applications*, vol. 29, no. 6, pp. 1135–1140, Nov 1993.

[17] Z. Qu, T. Tuovinen, and M. Hinkkanen, "Inclusion of magnetic saturation in dynamic models of synchronous reluctance motors," in *2012 XXth International Conference on Electrical Machines*, Sept 2012, pp. 994–1000.

[18] M. Hinkkanen, P. Pescetto, E. Mölsä, S. E. Saarakkala, G. Pellegrino, and R. Bojoi, "Sensorless self-commissioning of synchronous reluctance motors at standstill without rotor locking," *IEEE Transactions on Industry Applications*, vol. 53, no. 3, pp. 2120–2129, May 2017.

[19] Y. Murai, T. Watanabe, and H. Iwasaki, "Waveform distortion and correction circuit for pwm inverters with switching lag-times," *IEEE Transactions on Industry Applications*, vol. IA-23, no. 5, pp. 881–886, Sept 1987.

[20] A. R. Munoz and T. A. Lipo, "On-line dead-time compensation technique for open-loop pwm-vsi drives," *IEEE Transactions on Power Electronics*, vol. 14, no. 4, pp. 683–689, Jul 1999.

[21] R. B. Sepe and J. H. Lang, "Inverter nonlinearities and discrete-time vector current control," *IEEE Transactions on Industry Applications*, vol. 30, no. 1, pp. 62–70, Jan 1994.

[22] N. Mohan, T. M. Undeland, and W. P. Robbins, *Power Electronics. Converters, Applications and Design*, 3rd ed. John Wiley and Sons, Inc, 2003.

[23] J. K. Pedersen, F. Blaabjerg, J. W. Jensen, and P. Thogersen, "An ideal pwm-vsi inverter with feedforward and feedback compensation," in *1993 Fifth European Conference on Power Electronics and Applications*, Sept 1993, pp. 501–507 vol.5.

[24] J.-W. Choi and S.-K. Sul, "Inverter output voltage synthesis using novel dead time compensation," *IEEE Transactions on Power Electronics*, vol. 11, no. 2, pp. 221–227, Mar 1996.

[25] M. Sumner and G. M. Asher, "Self-commissioning for voltage-referenced voltage fed vector controlled induction motor drives," in *Power Electronics Specialists Conference, 1992. PESC '92 Record., 23rd Annual IEEE*, Jun 1992, pp. 139–144 vol.1.

[26] Y.-N. Lin and C.-L. Chen, "Automatic im parameter measurement under sensorless field-oriented control," *IEEE Transactions on Industrial Electronics*, vol. 46, no. 1, pp. 111–118, Feb 1999.

[27] A. Boglietti, P. Ferraris, M. Lazzari, and F. Profumo, "Induction motor equivalent circuit parameters determination from standard tests made with inverter supply," in *1993 Sixth International Conference on Electrical Machines and Drives (Conf. Publ. No. 376)*, Sep 1993, pp. 271–276.

[28] A. M. Khambadkone and J. Holtz, "Vector-controlled induction motor drive with a self-commissioning scheme," *IEEE Transactions on Industrial Electronics*, vol. 38, no. 5, pp. 322–327, Oct 1991.

[29] A. B. Proca and A. Keyhani, "Identification of variable frequency induction motor models from operating data," *IEEE Transactions on Energy Conversion*, vol. 17, no. 1, pp. 24–31, Mar 2002.

[30] J.-K. Seok, S.-I. Moon, and S.-K. Sul, "Induction machine parameter identification using pwm inverter at standstill," *IEEE Transactions on Energy Conversion*, vol. 12, no. 2, pp. 127–132, Jun 1997.

[31] M. Aiello, A. Cataliotti, and S. Nuccio, "A fully-automated procedure for measuring the electrical parameters of an induction motor drive with rotor at standstill," in *IMTC/2002. Proceedings of the 19th IEEE Instrumentation and Measurement Technology Conference (IEEE Cat. No.00CH37276)*, vol. 1, 2002, pp. 681–685 vol.1.

[32] G. Shen, K. Wang, W. Yao, K. Lee, and Z. Lu, "Dc biased stimulation method for induction motor parameters identification at standstill without inverter nonlinearity compensation," in *2013 IEEE Energy Conversion Congress and Exposition*, Sept 2013, pp. 5123–5130.

[33] S. H. Lee, A. Yoo, H. J. Lee, Y. D. Yoon, and B. M. Han, "Identification of induction motor parameters at standstill based on integral calculation," *IEEE Transactions on Industry Applications*, vol. 53, no. 3, pp. 2130–2139, May 2017.

[34] A. Bunte and H. Grotstollen, "Parameter identification of an inverter-fed induction motor at standstill with a correlation method," in *1993 Fifth European Conference on Power Electronics and Applications*, Sept 1993, pp. 97–102 vol.5.

[35] M. Ruff and H. Grotstollen, "Identification of the saturated mutual inductance of an asynchronous motor at standstill by recursive least squares algorithm," in *1993 Fifth European Conference on Power Electronics and Applications*, Sept 1993, pp. 103–108 vol.5.

[36] P. Castaldi and A. Tilli, "Parameter estimation of induction motor at standstill with magnetic flux monitoring," *IEEE Transactions on Control Systems Technology*, vol. 13, no. 3, pp. 386–400, May 2005.

[37] E. Levi, M. Sokola, and S. N. Vukosavic, "A method for magnetizing curve identification in rotor flux oriented induction machines," *IEEE Transactions on Energy Conversion*, vol. 15, no. 2, pp. 157–162, Jun 2000.

[38] A. Ganji, P. Guillaume, R. Pintelon, and P. Lataire, "Induction motor dynamic and static inductance identification using a broadband excitation technique," *IEEE Transactions on Energy Conversion*, vol. 13, no. 1, pp. 15–20, Mar 1998.

[39] M. Bertoluzzo, G. S. Buja, and R. Menis, "Self-commissioning of rfo im drives: one-test identification of the magnetization characteristic of the motor," *IEEE Transactions on Industry Applications*, vol. 37, no. 6, pp. 1801–1806, Nov 2001.

[40] A. V. Oppenheim and R. W. Schafer, *Discrete-Time Signal Processing*, 3rd ed. Prentice Hall Press, 2009.

[41] L. Peretti and M. Zigliotto, "Automatic procedure for induction motor parameter estimation at standstill," *IET Electric Power Applications*, vol. 6, no. 4, pp. 214–224, April 2012.

[42] J. Y. Ruan and S. M. Wang, "Magnetizing curve estimation of induction motors in single-phase magnetization mode considering differential inductance effect," *IEEE Transactions on Power Electronics*, vol. 31, no. 1, pp. 497–506, Jan 2016.

[43] S. A. Odhano, A. Cavagnino, R. Bojoi, and A. Tenconi, "Induction motor magnetizing characteristic identification at standstill with single-phase tests conducted through the inverter," in *2015 IEEE International Electric Machines Drives Conference (IEMDC)*, May 2015, pp. 960–966.

[44] K. Wang, W. Yao, B. Chen, G. Shen, K. Lee, and Z. Lu, "Magnetizing curve identification for induction motors at standstill without assumption of analytical curve functions," *IEEE Transactions on Industrial Electronics*, vol. 62, no. 4, pp. 2144–2155, April 2015.

[45] M. Carraro and M. Zigliotto, "Automatic parameter identification of inverter-fed induction motors at standstill," *IEEE Transactions on Industrial Electronics*, vol. 61, no. 9, pp. 4605–4613, Sept 2014.

[46] P. J. Turner, A. B. J. Reece, and D. C. Macdonald, "The dc decay test for determining synchronous machine parameters: measurement and simulation," *IEEE Transactions on Energy Conversion*, vol. 4, no. 4, pp. 616–623, Dec 1989.

[47] T. J. White and J. C. Hinton, "Compensation for the skin effect in vector-controlled induction motor drive systems," in *1995 Seventh International Conference on Electrical Machines and Drives (Conf. Publ. No. 412)*, Sep 1995, pp. 301–305.

[48] R. J. Kerkman, J. D. Thunes, T. M. Rowan, and D. W. Schlegel, "A frequency-based determination of transient inductance and rotor resistance for field commissioning purposes," *IEEE Transactions on Industry Applications*, vol. 32, no. 3, pp. 577–584, May 1996.

A Appendix: The Goertzel Algorithm

DFT of a finite-length sequence of length N is defined as

$$X[k] = \sum_{n=0}^{N-1} x[n] W_N^{kn} \quad k = 0, 1, ..., N-1 \tag{A1}$$

where $W_N = e^{-\mathrm{j}(2\pi/N)}$, $X[k]$ and $x[n]$ are sampled signal and its frequency-domain transformation, respectively. Computation can be reduced by taking the periodic nature of W_N^{kn} into account. For this purpose the starting point can be

$$W_N^{-kn} = e^{-\mathrm{j}(2\pi/N)Nk} = e^{\mathrm{j}2\pi k} = 1. \tag{A2}$$

Multiplying (A2) to (A1) gives

$$X[k] = W_N^{-kn} \sum_{r=0}^{N-1} x[r] W_N^{kr} = \sum_{r=0}^{N-1} x[r] W_N^{-k(N-r)}. \tag{A3}$$

The sequence can be defined as

$$y[n] = \sum_{r=-\infty}^{\infty} x[r] W_N^{-k(N-r)} u[n-r]. \tag{A4}$$

where by considering $x[n] = 0$ for $n < 0$ and $n \geq N$ and based on (A3) and (A4) it is obtained that

$$X[k] = y[n]\Big|_{n=N}. \tag{A5}$$

Expression (A4) can be defined as the convolution of the sequence $x[n]$, $0 \leq n \leq N-1$, with sequence of $W_N^{-kn} u[n]$ and $y[n]$ is the system response with the impulse response $W_N^{-kn} u[n]$ to the input $x[n]$. Furthermore, $X[k]$ is the output when $n = N$. The transfer function between the sequence $y[n]$ and the input $x[n]$ in Z-domain is

$$H(z) = \frac{1}{1 - W_N^{-k} z^{-1}}. \tag{A6}$$

Expression (A7) is achieved by multiplying $(1 - W_N^k z^{-1})$ to the numerator and denominator of (A6) as

$$H(z) = \frac{1 - W_N^{-k} z^{-1}}{(1 - W_N^{-k} z^{-1})(1 - W_N^{-k} z^{-1})} = \frac{1 - W_N^{-k} z^{-1}}{1 - 2\cos(2\pi k/N) z^{-1} + z^{-2}}. \tag{A7}$$

Figure A1 shows the Goertzel algorithm block diagram obtained by (A7).

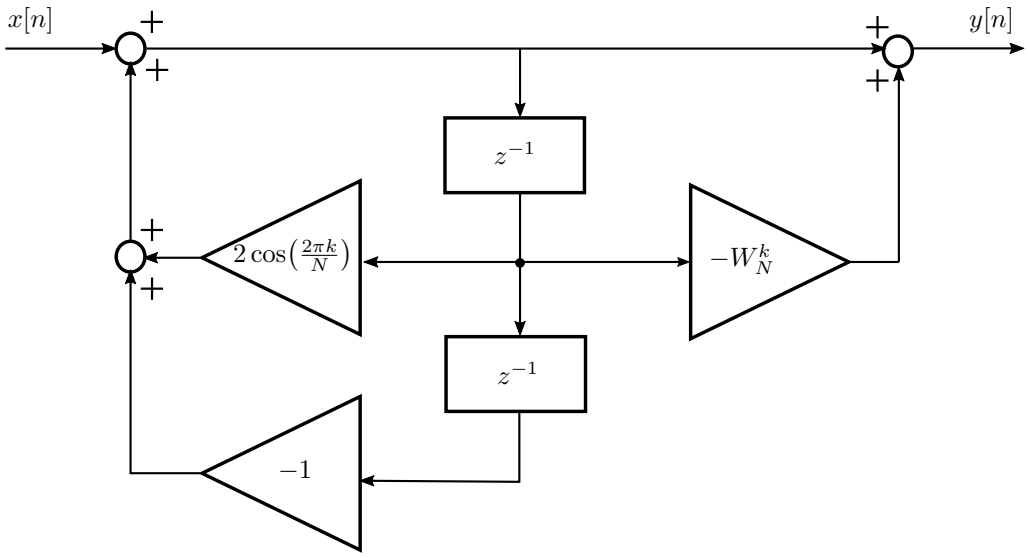

Figure A1: Block Diagram of the Goertzel algorithm.

B Appendix: LLS Fitting

Assuming the saturation function in (2.33), the inverse of the magnetizing inductance as a function of the stator flux is obtained as

$$\frac{1}{L_{\mathrm{M}}(\psi_{\mathrm{s}})} = c_0 + c_{\mathrm{s}}\psi_{\mathrm{s}}^S \tag{B1}$$

where the model is linear with respect to c_0 and c_{s}. The LLS problem in a vector form is

$$\underbrace{\begin{bmatrix} \frac{1}{L_{\mathrm{M}}(1)} \\ \frac{1}{L_{\mathrm{M}}(2)} \\ \vdots \\ \frac{1}{L_{\mathrm{M}}(N)} \end{bmatrix}}_{\boldsymbol{y}} = \underbrace{\begin{bmatrix} 1 & \psi_{\mathrm{s}}(1)^S \\ 1 & \psi_{\mathrm{s}}(2)^S \\ \vdots & \vdots \\ 1 & \psi_{\mathrm{s}}(N)^S \end{bmatrix}}_{\boldsymbol{X}} \underbrace{\begin{bmatrix} c_0 \\ c_{\mathrm{s}} \end{bmatrix}}_{\boldsymbol{\beta}} + \underbrace{\begin{bmatrix} \varepsilon(1) \\ \varepsilon(2) \\ \vdots \\ \varepsilon(N) \end{bmatrix}}_{\boldsymbol{\varepsilon}} \tag{B2}$$

where $\boldsymbol{y}$ is the vector of the inverse of the magnetizing inductance samples, $\boldsymbol{X}$ is the regressor matrix, $\boldsymbol{\beta}$ is the parameter vector, $\boldsymbol{\varepsilon}$ is the residual vector, and N is the number of samples. The sum of the squared residuals is

$$\boldsymbol{J}(\boldsymbol{\beta}) = \boldsymbol{\varepsilon}^T\boldsymbol{\varepsilon} = \sum_{n=1}^{N} \varepsilon(n)^2 \tag{B3}$$

where the parameter vector minimizing $\boldsymbol{J}$ is

$$\boldsymbol{\beta} = \left(\boldsymbol{X}^T\boldsymbol{X}\right)^{-1}\boldsymbol{X}^T\boldsymbol{y}. \tag{B4}$$

Fitting can be done for pre-selected values of the exponent S. Here, the exponent S is set to the value 7.